Pyroxenites and megacrysts from Vitim picrite-basalts (Russia): Polybaric fractionation of rising melts in the mantle?

I.V. Ashchepkov [a,*], L. André [b], H. Downes [c], B.A. Belyatsky [d]

[a] United Institute of Geology Geophysics and Mineralogy, SD RASc Novosibirsk, Russia
[b] Royal Museum of the Central Africa Tervuren, Belgium
[c] Department of Earth and Planetary Sciences, Birkbeck University of London, London, UK
[d] Institute of Precambrian Research, Russian Academy of Sciences, St. Petersburg, Russia

A B S T R A C T

Picrite basalt tuffs and lavas from the Miocene basalt plateau of Vitim (Trans Baikal, Russia) contain abundant megacrysts and varied pyroxenite and mantle lherzolite xenoliths (spinel facies and upper part of the garnet-facies) and crustal cumulates. Black pyroxenites and megacrysts show decreasing temperatures from 1350 to 900 °C, and range from high-T dark green websterites and clinopyroxenites, to low-T black megacrystalline garnet clinopyroxenites and phlogopite–ilmenite-bearing varieties. Garnet-bearing Cr-diopside veins and zoned veins with mica and rare amphiboles cross-cut peridotite xenoliths. Veins consisting of almost pure amphibole are more common in spinel lherzolite xenoliths. P–T calculations for pyroxenites yield pressure intervals at 3.3–2.3, 2.2–2.0, 1.9–1.5 and 1.3–1.0 GPa, probably corresponding to the locations of dense magmatic vein networks in mantle.

Major and trace elements for clinopyroxenes from the black megacrystalline series can be modeled by fractional crystallization of a picrite-basalt melt. In contrast, green high-temperature pyroxenites and black giant-grained garnet pyroxenites with lower LREE-enrichment and variable LILE and HFSE concentrations probably result from AFC processes and mixing with partial melts derived from older pyroxenites and peridotites. Gray low-Cr garnet clinopyroxenites with highly fractionated and inflected trace element patterns may have been formed by remelting of metasomatic veins within peridotites. Multistage melting of metasomatic assemblages with selective removal of clinopyroxene in vein contacts produce the REE patterns with low MREE concentrations and usually with elevated HFSE contents. Cr-diopside veins were most probably formed by partial melting of phlogopite- and/or amphibole-bearing lherzolites. The trace element and Sr–Nd isotopic features of the megacrystalline pyroxenites suggest that they crystallized from magma volumes that evolved in separate systems during formation of pre-eruption vein networks and magma chambers, which together formed the feeding system for the host basalts.

1. Introduction

Cognate relationships between suites of black pyroxenite (group II) xenoliths, megacrysts and their host basaltic lavas have been suggested by numerous authors (e.g., Beeson and Jackson, 1970; Wilshire and Shervais, 1975; Nixon and Boyd, 1979; Frey, 1980; Irving and Frey, 1984; Wilshire et al., 1980; Menzies et al., 1985; Liotard et al., 1988; Griffin et al., 1988; O'Reilly and Griffin, 1990; Liu et al., 1992; Righter and Carmichael, 1993; Dobosi and Jenner, 1999; Shaw and Eyzaguirre, 2000; Su et al., 2009, etc.), in part because of their geochemical features and similarity to experimental products (Knutson and Green, 1975; Edgar, 1987; Kogiso et al., 1998; Johnson, 1998; Yaxley, 2000). However, megacrysts tend to have less radiogenic $^{87}Sr/^{86}Sr$ ratios (e.g., Liotard et al., 1988; Akinin et al., 1997, 2005; Rankenburg et al., 2004, 2005) than their basaltic host rocks, which suggests that assimilation and fractional crystallization processes (AFC) (De Paolo, 1981; Neal and Davidson, 1989) or other types of interaction with mantle peridotite. Possible models of megacryst origin are: high pressure phenocryst crystallization; disintegration of high pressure coarse- and giant-grained pyroxenites (Irving, 1980) or growth in high pressure pegmatitic bodies (Rankenburg et al., 2005). Megacrystalline pyroxenites were probably formed during the ascent of the host magma to the surface (Lorand, 1989) and their crystallization may be a result of polybaric fractionation (Irving, 1984; Eggler and Mccallum, 1976; Neal, 1995) accompanied by AFC (Neal and Davidson, 1989).

Garnet peridotites and pyroxenite xenoliths and pyrope megacrysts are not frequent in alkali basalt (Beeson and Jackson,

* Corresponding author. Address: United Institute of Geology and Mineralogy, SD RASc, Academician V.A. Koptyug Avenue 3, 63090 Novosibirsk, Russia. Tel.: +7 383 2333584; fax: +7 383 2396452/2332792.
E-mail addresses: Igor.Ashchepkov@uiggm.nsc.ru, garnet@uiggm.nsc.ru, igora57@mail.ru (I.V. Ashchepkov).

1970; Chapman, 1976; Kepezhinskas, 1979; Nixon and Boyd, 1979; Delaney et al., 1979; Kovalenko et al., 1987; Mukhopadyay and Manton, 1994; Ashchepkov et al., 1996; Stern et al., 1999; Upton et al., 2003; Bjerg et al., 2005). The picrite-basalt tuffs from Vitim (Russia) and closely located volcanic centers (Ashchepkov et al., 2003) contain a nearly complete set of megacrysts, peridotites and pyroxenites as described in the literature. Thus their genetic relations and position in the mantle section can be deduced.

Megacrystalline pyroxenites are considered to be the source of the megacrysts found in the Vitim picrite-basalts (Ashchepkov and Andre, 2002). In this study we have investigated the origin of pyroxenites and megacrysts using a large collection of xenolithic material from Vitim (Ashchepkov et al., 1989, 1994; Ashchepkov, 2002; Ashchepkov et al., 2003; Ionov et al., 1993). Mineral grains from >400 pyroxenite xenoliths were analyzed by electron microprobe; about 50 monomineralic separates were analyzed by solution ICP-MS for trace elements, and several clinopyroxene separates were analyzed by TIMS for Sr–Nd isotope compositions. Glasses and minerals from the host picrite-basalts were also studied by LA ICP-MS for comparison.

2. Location and geology

Miocene to Pliocene basaltic plateaus and fields cover a huge area of Central Asia, Mongolia and Trans Baikal (Kiselev, 1987; Kepezhinskas, 1979; Dobretsov and Ashchepkov, 1991; Ionov et al., 1992, 1995; Ionov and Hofmann, 2007; Ashchepkov et al., 2003; Johnson et al., 2005). The Vitim basalt plateau was formed mainly in Miocene times, and is the largest of the Cenozoic plateaus in Trans Baikal. It is located in the loop of the Vitim river (Fig. 1), 250 km east of Lake Baikal (Ashchepkov et al., 1989; Ashchepkov, 2002). Most of the Miocene volcanoes, the basal flows of the Vitim plateau, and the Plio-Pleistocene cinder cones and post-erosion lava flows, contain mantle and crustal xenoliths (Ashchepkov et al., 1989, 1994, 2003; Ionov et al., 1993, 2005a,b).

The pyroxenite xenoliths analyzed in this study were all collected from picrite-basalt tuffs excavated in a road quarry 1.5 km NE of the Vereya stream at the 75 km marker (N 53.742, E 113.336). The age of the tuffs is uncertain (13.5–18.5 Ma) due to the presence of abundant debris of crustal rocks, but they may be related to basalts and tuffs exposed nearby that were dated at 13–14 Ma (Ashchepkov et al., 1989, 2003). The tuffs contain mantle xenoliths up to 40 cm in diameter and abundant xenocrysts. The xenolith suite consists of garnet lherzolite (65%), spinel lherzolite (15%), black megacrysts and their giant-grained intergrowths (~15%), green Cr-diopside websterites (5%), gray pyroxenites that are transitional between the black and green varieties, black fine-grained pyroxenites and lherzolites veined by pyroxenites (~1–3%). The nearby (Fig. 1) Pliocene and Pleistocene volcanoes Kandidushka (N 53.834, E 113.357) and Yaksha (N 53.719, E 113.339), dykes at Bulykhta (N 53.725, E 113.258) and associated lava flows (N53.771, E 113.249) along the Dzhilinda river also contain mantle xenoliths (Ashchepkov et al., 2003) but these are not described in this paper.

3. Petrography

The general division into green Cr-diopside-bearing pyroxenite suites (group I) and black Al-augite-dominated suites (group II), advocated by Wilshire and Shervais (1975) and Frey and Printz (1978), allows us to separate the Vitim megacrysts and pyroxenites into two large groups. However, below we present a more detailed division, taking into account their petrographic features, and major and trace element mineral chemistry (Table 1). The samples were first divided using varimax factor analyses using major element compositions as described by Ashchepkov et al. (1994). Division into the groups was later supported by trace element data that show correlations between PT parameters and degree of differentiation (Ashchepkov et al., 1995b; Litasov et al., 2000; Ashchepkov and Andre, 2002), using the same set of major element analyses,
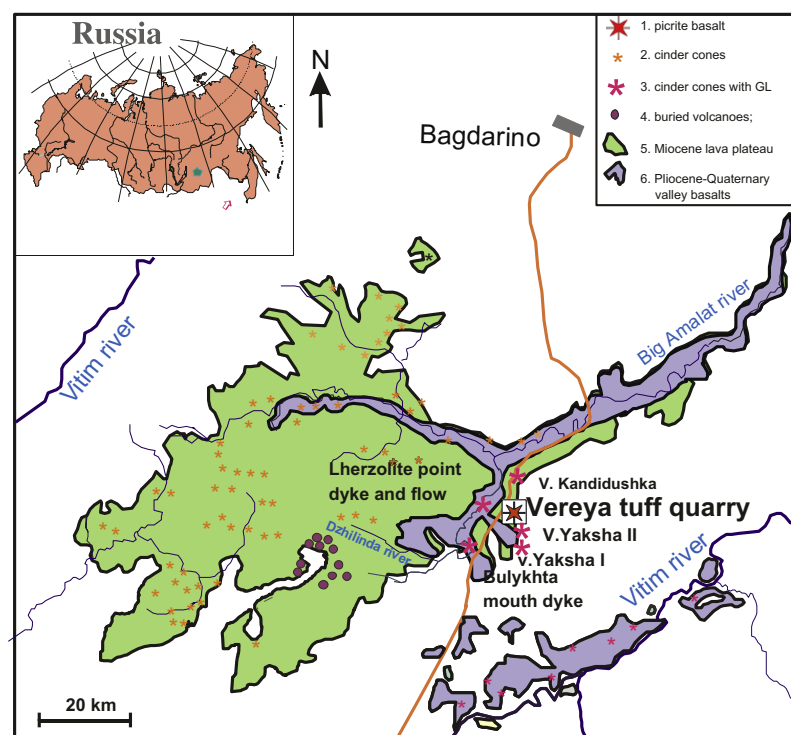

Fig. 1. Schematic map of the Vitim plateau basalts. (1) Buried volcanoes; (2) cinder cones; (3) Miocene lava plateau; (4) Pliocene-Quaternary valley basalts.

Table 1
Major and trace element compositions of minerals from deep seated xenoliths from Vitim basalts.

Name of group	Petrographic composition	Major element chemistry of clinopyroxenes (in wt.%)	Trace element characteristics of Cpx	Suggested origin	Proportion of xenoliths (%)
Black megacrystalline pyroxenites (BMP)	Cpx + Gar + minor Opx	FeO = 7–8.5; Na_2O = 1.3–2.3; TiO_2 = 0.3–0.7; Al_2O_3 = 5.5–6.5	Primitive REE and trace elements with lower Ta, Nd, Th ,U and LILE	Magma chambers and feeders of picrite basalt	5
Subgroup black megacrystalline pyroxenites (BMG)	Cpx + minor Gar + Opx	FeO = 7–11; Na_2O = 2–3.8; TiO_2 = 0.8–2; Al_2O_3 = 7–9	The same elevated (does this mean "same pattern but higher overall values"?)	Feeder vein and lower magmatic chamber	8.5
Subgroup (BM1)	Cpx + minor Gar + Opx in Cr-bearing varieties	FeO = 7–8.5; Na_2O = 2–2.5; TiO_2 = 0.8–1.2; Al_2O_3 = 7–8	same pattern but higher overall values	Feeder vein and clot referring to small intermediate chamber	7
Subgroup (BM2)	Cpx	FeO = 8–8.5; Na_2O = 2–2.5; TiO_2 = 1.3–1.5; Al_2O_3 = 8–9	The same elevated	Feeder vein	4
Ilmenite-bearing subgroup (BMI)	CPx + Ilm + minor Phl	FeO = 9–10; Na_2O = 2–3; TiO_2 = 1.3–1.5; Al_2O_3 = 8–9	The same elevated. Higher LILE	Feeder vein, showing degassing and oxidation	0.05
Subgroup of kelyphitic pyroxenes (BMK)	Cpx + minor Ilm	FeO = 9.5–11; Na_2O = 3–3.5; TiO_2 = 1.5–1.8; Al_2O_3 = 8–9	The same elevated. Higher LILE	Branching feeder vein at the top of mantle column, degassing	0.45
Green clinopyroxenites (DGC) low Cr	Cpx	FeO = 5–6; Na_2O = 1–1.5; TiO_2 = 0.2–0.5; Al_2O_3 = 5–6.3	The same elevated. Higher LILE	Early magma chamber of contaminated picrite – basalt melt	0.5
Dark green coarse-grained websterites (DGW)	Cpx + Opx	FeO = 6–7.8; Na_2O = 1.25–1.5; TiO_2 = 0.2–0.7; Al_2O_3 = 6–7	The same elevated.	Early magma chamber of contaminated picrite – basalt melt	1
Gray transitional (in Cr) garnet clinopyroxenites (GGP)	Gar + Cpx	FeO = 3.8–5.3; Na_2O = 1.8–2.5; TiO_2 = 0.1–0.5; Al_2O_3 = –9	Inflected REE and higher La/Yb_n than in BM	Remelted amphibole-bearing metasomatites	2
Veined orthopyroxenites and websterites with kaersutite, mica, ilmenite and garnet-bearing pyroxenites (VAPP)	Cpx + Gar + Kaers + Phl + Opx + Sp + llm	FeO = 4.75–7; Na_2O = 1.3–2.5; TiO_2 = 0.1–1.5; Al_2O_3 = 5–8	Very high trace element abundances, but low HFSE, very high LILE	Veins of differentiated picrite basalt melts in garnet and spinel lherzolites	1
Fine-grained garnet- plagioclase-clinopyroxene cumulates (LPC)	Pl + Cpx + Gar + Opx + Sp + llm + Mgt + Kaers + Phl	FeO = 7–12; Na_2O = 0.5–2; TiO_2 = 0.5–2; Al_2O_3 = 5–9	Very high level LILE, but low HFSE	Cumulates of contaminated basalts in lower crust	3
Cr-diopside emerald-green pyroxenite veins (CDP)	Cpx + Gar + Opx + Ol + minor Sp + Phl	FeO = 2.3–4.5; Na_2O = 1–2.5; TiO_2 = 0.25–1.5; Al_2O_3 = 4.5.–9	Primitive REE and trace elements, sometimes with elevated HFSE	Partial melts in lherzolite partly formed under influence of volatiles from basalts	5
Garnet lherzolites (GL)	Ol + Cpx + Gar + Opx + Sp + Phl + Parg	FeO = 2.3–4.5; Na_2O = 1–2.3; TiO_2 = 0.25–1; Al_2O_3 = 4.5–7	Primitive REE and trace elements,with fluctuations of LILE	Mantle diapir from convective mantle	55
Spinel lherzolites (SL)	Ol + Cpx + Opx + Sp + Phl + Parg	FeO = 1.9–3.5; Na_2O = 0.8–2; TiO_2 = 0.2–0.8; Al_2O_3 = 3–5	Flattened REE and trace elements,with fluctuations of LILE and HFSE	Old lithospheric mantle	10

suggested separation of the Vitim pyroxenites into seven groups, mainly repeating the previously established classification by Ashchepkov et al. (1994) which is used in this present study. Fig. 2 shows the typical appearance of the Vitim pyroxenites in hand specimen.

3.1. Black megacrystalline pyroxenites (BMP)

Megacrystalline clinopyroxene aggregates with large (3–10 cm and more) rounded or curved grains (Fig. 2-1 and -2) are similar in appearance to the individual black pyroxene megacrysts. In the coarse-grained varieties, rounded garnet grains (3–5 cm) occur with orthopyroxenes in the intergranular space or in the rims of large augite crystals. These garnet-bearing black pyroxenites are designated as BMG. Several types of black megacrysts contain abundant dispersed pyrrhotite grains and, more rarely, elongated ilmenite grains. Rare deformed varieties (sample 315-73) (Fig. 2-1) contain crushed garnet aggregates (up to 30–45% of xenolith volume), mostly altered to kelyphite (Pl-Sp-Opx), which cements the chains of larger rounded deformed clinopyroxene grains. An unusual clinopyroxene druse (sample 315-410) (Fig. 2-3) similar to those found in Mongolia (Kovalenko et al., 1987) consists of
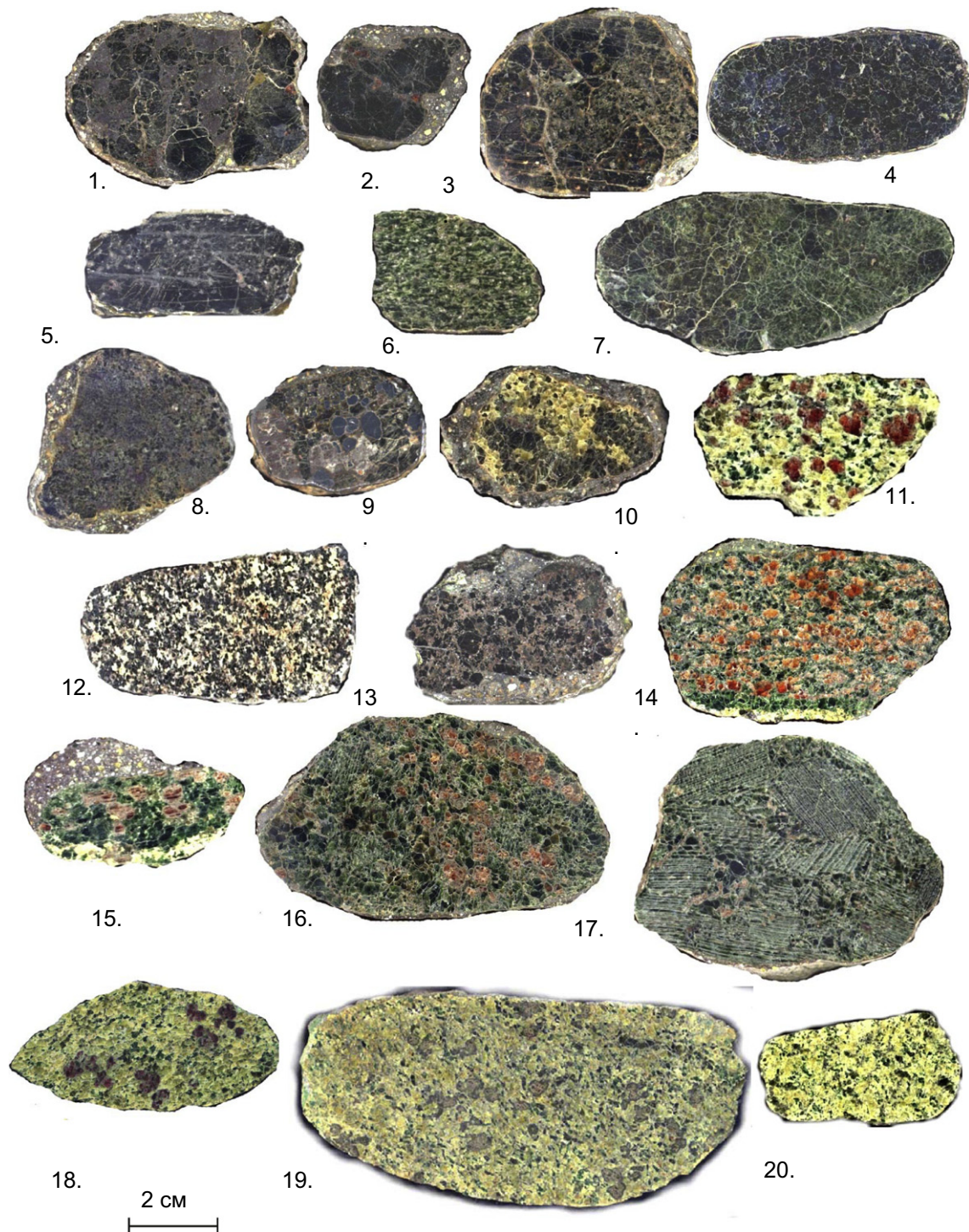
Fig. 2. Images of pyroxenite xenoliths from Vitim picrite basalts. (1) Black garnet pyroxenite (BMG) with crushed garnet aggregate cementing the cage of the large clinopyroxene grains. (2) Black garnet pyroxenite (BMG) with intergranular garnet. (3) Druse of partly broken black megacrystalline (BM1) augite crystals cemented by a later generation of the same mineral with abundant gaseous cavities. (4) Medium-grained grained black clinopyroxenite (BM2). (5) Black megaclinopyroxenite with small ilmenite (BMI) inclusions. (6) Dark green clinopyroxenite (DGC) with poikilitic orthopyroxene inclusions and fluid cavities. (7) Dark green websterite (DGW). (8) Deformed transitional high temperature garnet websterite (GGP). (9) Gray garnet websterites (GGP) with rounded ilmenite blebs at the contact with peridotites represented by an aggregate of orthopyroxene and garnet rimmed with plagioclase. (10) Garnet veined pyroxenite (VAPP) with kaersutite and mica in contact with lherzolite. Garnet and smaller kaersutite and clinopyroxene grains are distributed in the contacts. (11) Phlogopite veinlets in coarse-grained garnet lherzolite (GL). (12) Plagioclase clinopyroxenite with rare orthopyroxenes, abundant magnetite and ilmenite (LPC). (13) Kaersutite–Ti-biotite coarse-grained vein in augite-plagioclase aggregate (veined LPC). (14) Green Cr-diopside garnet websterite (CDP) in contact with garnet lherzolite. (15) Green Cr-diopside garnet clinopyroxenite (CDP) in contact with lherzolite. (16) Garnet-bearing Cr-diopside websterite (CDP) with garnet-orthopyroxene lamellae in the larger rounded clinopyroxene grains. (17) Garnet Cr-diopside clinopyroxenite (CDP) with the garnet inclusions and garnet orthopyroxene lamellae in clinopyroxene grains. (18) Nearly equigranular garnet lherzolite (GL) enriched in pyroxenes and dunite vein. (19) Large xenoliths of deformed garnet lherzolite (25×12 cm) with signs of plastic flow. (20) Coarse-grained spinel lherzolite (SL). (For interpretation of the references to colour in this figure legend, the reader is referred to the web version of this article.)

large euhedral or partly broken crystals (1–2 cm). The space between the large primary crystals is filled by clinopyroxenes with abundant scattered cracks which contain decrepitated fluid inclusions and gaseous blebs often connected in channels. Such garnet-free varieties with gas cavities and brownish color are referred to as subgroup BM1 (Fig. 2-4), whereas the black monocrystals without gaseous blebs form subgroup BM2. The ilmenite-bearing subgroup (here termed "BMI") contains elongated small or rounded ilmenite grains together with Ti-biotite grains (up to 0.75 cm) and sometimes sulfides (Anderson et al., 1987) incompletely filling the cavities (Fig. 2-5). Pyroxene grains with abundant inclusions are often altered to aggregates of secondary pyroxenes, oxides and glass. Xenoliths with highly altered (kelyphite-like) giant pyroxene blocks (up to 20 cm) form another subgroup, termed "BMK". Sometimes contacts between the BM rocks and dark gray garnet-bearing pyroxenites resemble 'dyke in dyke' or 'vein in vein' structure.

3.2. Dark green coarse-grained websterites (DGW) and green clinopyroxenites (DGC)

The large dark green clinopyroxene grains (up to 3–5 cm) are sometimes partly broken and have exsolution lamellae of orthopyroxene in their margins and also contain rounded orthopyroxene inclusions and gaseous cavities (Fig. 2-6). Websterites (Fig. 2-7) have typical grain sizes of 1–2 cm, contain more orthopyroxenes and are more homogeneous. Usually these bi-mineralic rocks are similar in appearance and texture to the BMP group but are green or brownish-green in color.

3.3. Gray garnet clinopyroxenites (GGP)

Gray garnet clinopyroxenites usually contain kelyphitic garnets (Fig. 2-8). In rare cases crushed pyroxenites are in contact with black clinopyroxene megacrysts. Greenish-gray megacrystalline clinopyroxenites sometimes contain kaersutite, ilmenite and garnet grains, surrounded by anorthoclase (Fig. 2-9) (sample 315-446). Symplectitic aggregates of Fe–Mg spinel, orthopyroxene and plagioclase in intergranular spaces are similar to those described by Huang et al. (2007) from China. There are two types: a coarse-grained group composed of clinopyroxene and garnet, and a polymineralic fine-grained subgroup which contains inclusions of orthopyroxene and ilmenite.

3.4. Veined pyroxenites with amphibole and phlogopites (VAPP)

Veined aggregates occur on the outer contacts of thick kaersutite-clinopyroxenite veins that cut peridotites (Fig. 2-10). They display regular variations in grain sizes, morphology and mineral compositions. Zoned varieties cutting garnet lherzolites contain mica veins (Ionov et al., 2005a,b) which are rimmed by zones of kaersutite, clinopyroxene and orthopyroxene (sample 315-414). Glass pockets with amphiboles (Glaser et al., 1999) and newly formed Cr-diopsides and Cr-spinels occur around them. They may also be found in separate peridotite xenoliths. Veins cutting spinel lherzolites are essentially kaersutitic, while garnet lherzolites contain monomineralic phlogopite veinlets (Fig. 2-11). Monomineralic pargasite microveins and pockets in lherzolites surround the contacts of the VAPP rocks at a distance of ~3–7 cm.

3.5. Fine-grained low pressure cumulates (LPC)

These relatively pale rocks are composed of garnet, plagioclase and clinopyroxene and show cumulative structures (Fig. 2-12) and sometimes gaseous blebs and glasses in their walls and in intergranular space; they frequently show mineral layering typical

of lower crustal basaltic cumulates (Downes, 1993; Rudnick and Fountain, 1995; Zheng et al., 2009). They are crossed by veins of kaersutite and Ti-biotite with intergranular plagioclase (Fig. 2-13) that contain large amounts of ilmenite or magnetite.

3.6. Cr-diopside emerald-green pyroxenite veins (CDP)

Green pyroxenites vary in appearance, modal composition and texture and can have either sharp or gradual contact relations with their host lherzolites (Fig. 2-14, 15). Garnet clinopyroxenites can sometimes be deformed to mylonites at their contacts with lherzolites (Fig. 2-15). The monomineralic rims in the contacts suggest a reaction relationship (Fig. 2-11). The hydrous veins have contact assemblages that are essentially orthopyroxenite. Lamellae of garnet and orthopyroxene in the large clinopyroxene grains may be a result of exsolution (Huang et al., 2007) (sample 315-253) (Fig. 2-16). Small rounded garnet grains with orthopyroxene and clinopyroxenes are also present in pegmatite-like intergrowths (Fig. 2-17). In large samples, such grains are cemented by homogeneous garnet and pyroxene grains with the same composition (sample 315-253) (Fig. 2-16). Garnet coronas occur around large spinels. Sometimes the garnet-spinel relations and grain-sizes change gradually across the sample.

3.7. Garnet lherzolites (GL) and spinel lherzolites (SL)

Garnet lherzolites (GL) were described in previous publications (Ashchepkov et al., 1989, 1994; Ionov et al., 1993; Glaser et al., 1999). They have protogranular textures with wide variations in grain sizes and mutual relationships between constituent minerals. The garnets usually form large crystals (Fig. 2-19) and rounded grains in the olivine matrix; there are also fine-grained nearly equigranular lherzolites unusually enriched in pyroxenes and garnets. Foliation is common (Fig. 2-18). Rare sheared varieties are found at the contacts between lherzolites and Cr-diopside pyroxenites (Ashchepkov et al., 2003). Spinel lherzolites (SL) contain more olivine and orthopyroxene and are coarser-grained (Fig. 2-20). They differ from GL in having lower modal pyroxene abundances (Ashchepkov et al., 1994; Ionov et al., 2005a,b), but in general they are more fertile than SL from most localities in Europe (Witt-Eickschen and Kramm, 1998; Witt-Eickschen et al., 2003; Upton et al., 1999, 2003; Downes, 2001) and North America (Wilshire and Shervais, 1975).

4. Analytic procedures

4.1. Electron microprobe analyses

Most analyses were obtained at the Institute of Geology and Geophysics (Novosibirsk) using a CamebaxMicro electron microprobe. All analyses were made in wavelength-dispersive (WDS) mode using a variety natural reference minerals and synthetic glasses for calibration (Lavrent'ev et al., 1987). The accelerating voltage was 15 kV and a focused beam of 15 or 20 nA was used. Reduction procedure using "Karat program" (Lavrent'ev and Usova, 1994) was applied to the analyses. The relative standard deviation does not exceed 1.5%, the precision was close to 0.02–0.015% for minor elements. Detailed microprobe analyses of several xenoliths were obtained in Leuven University (Belgium) on a CAMECA50SX using mainly synthetic glasses for calibration and the PAP (Pouchou and Pichoir, 1984) method of data reduction. The analytical method was similar but accuracy was better due to better microprobe stability. Analyses of the same grains made by the two instruments gave practically the same results. The grains are mostly homogeneous as was checked by the profiles of the large

grains and by an autoradiographic method (Dobretsov et al., 1992), except for some large BMG xenoliths like 315-222 (see supplemental file 1) and veined pyroxenites.

4.2. ICP-MS analyses

Trace elements were determined by solution ICP-MS in the Royal Museum for Central Africa in 1993–1994. Hand-picked separates of pyroxenes, garnets and amphiboles were leached in three stages: 15 min with concentrated HCl; 15 min with dilute (5%) HF; and 15 min with concentrated HF. For phlogopites, the leaching procedure was limited to the first two stages. About 0.1 g of leached minerals was completely digested in a mixture of three Suprapur® Merck acids (HF:4 g; HNO3:1 g; HClO$_4$:1 g) in a Teflon vessel heated at 180 °C for 3 days in an autoclave. Then each sample was dried in the presence of excess HClO$_4$ in order to avoid any precipitates of fluorides or fluorosilicates. After complete removal of HF, the sample was evaporated to dryness, and the remaining solid was next dissolved in HNO$_3$. The solution was then transferred into 50 ml volumetric flasks and made to volume with a 5% nitric acid solution with a reference quantity of four internal tracers (Ru, In, Re, Bi). The instrument used was a VG elemental Plasmaquad® (PQ 2 Turbo Plus) ICP-MS equipped with a V-Groove de Galan nebuliser and a chilled spray chamber (5 °C) and operated at an Ar flow-rate of 0.755 l/min. The ICP-MS was optimized with a 10 ppb solution of ^{59}Co, ^{115}In and ^{238}U in order to obtain a typical sensitivity of 5×10^4 counts s^{-1} ppb^{-1} on ^{115}In. Each sample was measured in triplicate with a reagent blank subtraction and interference oxide corrections of ^{135}Ba^{16}O on ^{151}Eu, ^{141}Pr^{16}O on ^{157}Gd, ^{147}Sm^{16}O on ^{163}Dy, ^{149}Sm^{16}O on ^{165}Ho and ^{165}Ho^{16}O on ^{181}Ta. Data were acquired in peak jumping mode with three points by peak, using a pulse counting detector type and an acquisition time of 80 s. Mass-sensitive drifts linked to matrix effects and changes in instrumental parameters were continuously monitored by measuring fluctuations of ^{99}Ru, ^{115}In, ^{185}Re and ^{209}Bi signals from the sample solution. Potential drift in the oxide levels were monitored at the mass 248(^{232}Th^{16}O).

Element concentrations were obtained using a double external calibration with five international standards (PCC-1, DTS-1, AN-G, W1, BHVO-1, digested and prepared as the samples) and four artificial standards (Andre and Ashchepkov, 1996). Detection limits vary between 0.4 ppb for Lu to 700 ppb for Sc (calculated for solid matter) (Table 2). The reproducibility, tested on solution duplicates, ranged between 0.2% and 3% for all the analyzed elements. Precision of the whole method (sum of sample + weighing + digestion + dilution + analyses reproducibility), at the measured low concentrations, was determined using three replicate analyses of four different clinopyroxenes; it was excellent (1–5%) for all REE, Sr and Co, good (5–15%) for Sc, Cu, Zn, Ge, Rb, Zr, Nb, Y, U and Th, fair (15–25%) for Ba, Hf, Ta and Pb, but rather poor for Cs (50%) due to the extremely low concentration. This large replicate database demonstrates both sample homogeneity and analytical precision. The accuracy of the method has been checked by running three international standards (NIM-D, NIM-N, UB-N) (see supplemental file 2) (Govindaraju, 1988a,b; Verma et al., 1992; Andre and Ashchepkov, 1996) with the samples. The LA-ICP-MS data for glasses and minerals from picrite-basalts were obtained using the same VG Elemental Plasma Quad (PQ2 Turbo Plus) ICP-MS (Musée Royal de l'Afrique Centrale, Tervuren) coupled with a UV Fisons laser ablation microprobe based on a continuum Minilite Q-switched Nd:YAG laser operating in the far-UV (266 nm) wavelength. The power of the output beam is maximum (2 mJ/pulse) for a 10 Hz repetition rate of pulse. The precision and description of method were published (Brassinnes et al., 2005).

4.3. ^{143}Nd/^{144}Nd and ^{87}Sr/^{86}Sr isotopic analyses

Sr and Nd isotopic ratios for clinopyroxenes from several Vitim pyroxenite xenoliths were obtained at the Institute of Precambrian Research, Russian Academy of Sciences, in St. Petersburg. Approximately 50–100 mg of the sample was placed into closed quartzglass and leached by dilute HNO$_3$ on a hot plate for 15 min. The sample was dried and crushed in a jasper mortar, weighed, spiked in Teflon bombs with mixed ^{146}Nd-^{149}Sm and ^{84}Sr-^{85}Rb spikes and dissolved over 2–5 days in a mixture of HF + HNO$_3$ + HClO$_4$ at 120 °C. Rb, Sr, Sm and Nd separation was carried out by a two-stage cation-exchange and extraction chromatography (Richard et al., 1976) removing the matrix elements in the first stage. Measurements were performed on a Finnigan MAT-261 thermal ionization mass spectrometer equipped with 8-collectors under static mode. The ^{143}Nd/^{144}Nd ratio was normalized within-run to ^{148}Nd/^{144}Nd = 0.241570 and then adjusted to a ^{143}Nd/^{144}Nd value of 0.511860 for the La Jolla international standard. Sr isotope composition was normalized within-run to ^{88}Sr/^{86}Sr = 8.37521. The value of Sr isotope standard SRM-987 analyzed during this work was ^{87}Sr/^{86}Sr = 0.710248 ± 15 (2σ, 6 runs). Assigned errors (2σ) for ^{147}Sm/^{144}Nd and ^{143}Nd/^{144}Nd were ±0.3% and ±0.000015, respectively, ^{87}Rb/^{86}Sr ± 0.5%, ^{87}Sr/^{86}Sr ± 0.000025 according to results of multiple analyses of standard (external reproducibility). The 2σ errors for ^{143}Nd/^{144}Nd and ^{87}Sr/^{86}Sr (Table 3) reflect in-run precision and demonstrate the quality of these analyses. Blanks are as follows: 0.01 ng Sm, 0.05 ng Nd, 0.05 ng Rb and 0.2 ng Sr. The data obtained for BCR-1 during the course of this analytical work are: [Sr] = 335.8 ppm, [Rb] = 47.16 ppm, [Sm] = 6.487 ppm, [Nd] = 28.45 ppm, ^{87}Sr/^{86}Sr = 0.705053 ± 11, ^{87}Rb/^{86}Sr = 0.40615, ^{143}Nd/^{144}Nd = 0.512663 ± 9, ^{147}Sm/^{144}Nd = 0.13829.

5. Major element chemistry variation in clinopyroxene

The Al-augite black megacrystalline pyroxenites (BMP) from Vitim form a petrographic sequence DGW–DGC–BGM–BM1–BM2–BMK–VAPP–LPC, varying from essentially orthopyroxene- to garnet- then to ilmenite-bearing lithologies, and then to those with mica and plagioclase ± kaersutite (Table 1, supplemental file 1). TiO$_2$, Na$_2$O, Al$_2$O$_3$ and CaO values in the clinopyroxene increase with increasing Fe#s, separating in subgroups, arrays and trends (Fig. 3).

Crystallization started with the clinopyroxenes of the DGW group (group II of Litasov et al., 2000) which contain 4.9 wt.% FeO and up to 0.7% Cr$_2$O$_3$ and have the lowest TiO$_2$, Na$_2$O and Al$_2$O$_3$ contents. The next group (DGC) continues the trends (Fig. 3) with an inflection to typical black pyroxenites. The BMG clinopyroxenes define a distinct line from 7 to 8.5 wt.% FeO with increasing TiO$_2$ and Al$_2$O$_3$ concentrations. Deviations to lower Na$_2$O, Al$_2$O$_3$ and TiO$_2$ values in clinopyroxenes correspond to the appearance of orthopyroxene and a decrease in grain-size. Clinopyroxenes enriched in FeO, Na$_2$O and TiO$_2$. (referred to as BM1) are located above the BMG in the FeO-TiO$_2$ plot. The next cluster (referred to as BM2) is connected with the BM1 cluster by a narrow chain of points. Clinopyroxenes from the most enriched pyroxenite varieties containing ilmenites and phlogopites (BMI) form a branch with lower FeO content (∼9 wt.%), whereas clinopyroxenes from the BMK group are extremely enriched in FeO (up to 11 wt.%) (see Table 1).

Low-Cr (0.1–0.3 wt.%), Al-rich clinopyroxenes with ∼3.5–4.5 wt.% FeO belong to the gray garnet clinopyroxenite (websterite) suite (GGP) or IIc subgroup according to Litasov et al. (2000) and form a separate trend intermediate CDP or BM varieties. Clinopyroxenes from the veins of phlogopite- and amphibole-rich pyroxenites (VAPP) vary in composition and form three groups

Table 2
Major and trace element compositions of minerals from deep seated xenoliths from Vitim basalts.

Rock type	Green HT pyroxenite		Dark green HT pyroxenite			Black Ga megapyroxenite			
Element	315-13Cpx	315-104 Cpx	315-117 Cpx	315-116 Cpx	315-254 Cpx	315-254 ga	315–73 Cpx	315-184 Cpx	315-184 ga
SiO$_2$	51.80	52.59	51.30	52.16	50.73	41.48	50.71	51.15	41.19
TiO$_2$	0.36	0.33	0.53	0.42	0.63	0.38	0.75	0.666	0.425
Al$_2$O$_3$	6.52	5.07	7.25	5.56	7.54	22.62	7.02	7.1	22.6
Cr2O3	0.56	0.77	0.13	0.37	0.02	0.05	0.03	0.031	0.08
FeO	6.06	4.80	7.41	6.07	7.57	12.45	7.70	8.02	13.57
Mn	0.10							0.131	0.328
MgO	19.22	19.58	17.40	17.74	15.46	17.60	14.93	16.45	17.3
CaO	12.67	15.10	13.79	15.79	15.10	5.07	15.06	14.59	5.07
Na$_2$O	1.49	1.06	1.62	1.20	1.97	0.11	2.39	1.73	0.053
K$_2$O						0.63			0.003
Total	98.78	99.30	99.43	99.31	99.64	99.76	99.35	99.87	100.62
Ba	3.63	5.16	1.44	1.78	2.25	0.64	2.08	4.70	0.64
La	1.04	1.54	1.02	1.20	1.21	0.05	1.32	1.77	0.04
Ce	3.62	5.24	3.81	4.39	4.40	0.26	4.19	6.42	0.20
Pr	0.69	0.93	0.72	0.80	0.88	0.09	0.79	1.21	0.07
Nd	4.05	4.91	4.14	4.45	5.03	0.97	4.63	6.89	0.92
Eu	0.49	0.55	0.58	0.58	0.67	0.71	0.57	0.92	0.59
Sm	1.33	1.51	1.51	1.54	1.72	1.11	1.49	2.43	0.98
Gd	1.58	1.56	1.79	1.70	2.10	3.75	1.98	2.75	3.32
Dy	1.47	1.32	1.73	1.62	1.75	9.24	1.75	2.39	7.38
Ho	0.28	0.24	0.32	0.30	0.32	2.49	0.32	0.42	1.97
Er	0.70	0.57	0.74	0.71	0.71	8.54	0.71	0.90	6.24
Yb	0.56	0.39	0.48	0.50	0.44	9.35	0.50	0.49	7.01
Lu	0.077	0.045	0.054	0.059	0.056	1.370	0.062	0.048	1.060
Hf	0.65	0.49	0.65	0.63	0.92	1.12	0.91	0.93	0.80
Ta	0.116	0.001	0.005	0.010	0.029	0.255	0.069	0.009	0.00
Pb	0.13	0.08	0.05	0.05	0.19	0.11	0.55	0.12	0.04
Th	0.05	0.04	0.02	0.03	0.02	0.01	0.05	0.04	0.00
U	0.02	0.01	0.00	0.01	0.01	0.01	0.00	0.00	0.00
Sc	23.0	25.5	17.6	22.9	22.3	89.8	24.0	12.9	89.7
V					391				
Co	38.9	29.4	35.2	35.4	52.8	62.5	56.6	36.4	81.4
Cu	13.04	3.78	5.96	10.5	22.10	8.40	12.05	5.34	2.76
Zn	21.5	20.8	33.1	32.9	43.3	26.6	50.2	36.9	40.9
Rb	0.17	0.15	0.12	0.11	0.24	0.09	0.13	0.19	0.00
Sr	52	64	52	54	63	1.5	68.2	65.1	1.1
Y	4.41	5.40	7.55	7.49	7.28	46.20	8.29	7.98	56.09
Zr	8.20	12.8	16.5	16.9	24.6	27.9	18.6	22.9	37.8
Nb	0.34	0.20	0.15	0.18	0.28	0.11	0.49	0.27	0.09
Cs	0.001	<0.01	<0.01	<0.01	0.003	0.000	0.008	<0.01	0.001

	Black Megapyroxenite		Black Megapyroxenite		Black Ilm-Phl Megapyroxenite			Phl-Kaers-Pyroxenite	
Element	315-174Cpx	315-167Cpx	315-133Cpx	315-161Cpx	315-340Cpx	315-340phl	315-341phl	315-440Cpx	315-440phl
SiO$_2$	49.87	49.55	49.22	49.55	49.43	36.91	36.21	51.04	36.82
TiO$_2$	1.30	1.49	1.51	1.54	1.64	8.41	8.67	1.00	8.48
Al$_2$O$_3$	7.95	8.06	8.90	8.69	8.23	15.67	14.89	6.25	13.68
Cr2O3	0.00	0.02	0.00	0.00	0.01	0.01	0.00	0.42	0.53
FeO	8.84	9.24	10.29	10.67	8.41	12.32	13.09	4.82	8.15
Mn									
MgO	13.20	12.73	9.83	9.91	11.87	14.10	13.42	13.47	16.71
CaO	15.78	15.67	15.83	15.76	15.46	0.21	0.16	20.44	0.00
Na$_2$O	2.50	2.61	3.31	3.57	3.42	0.11	0.07	1.67	0.37
K$_2$O	1.30	1.49	1.51	1.54		6.26	7.07	0.00	9.54
F						0.46	0.34		
Cl						0.02	0.04		
Total	100.74	100.86	100.40	101.23	98.47	94.48	92.97	99.11	94.27
Ba	4.12	3.23	24.38	8.77	6.79	4374.	4834.	5.07	11,535
La	1.61	1.83	2.20	2.42	2.01	0.24	1.08	2.26	0.29
Ce	6.22	6.90	8.26	9.32	7.60	0.41	2.23	16.02	0.99
Pr	1.24	1.38	1.63	1.85	1.53	0.06	0.35	3.85	0.19
Nd	7.25	8.52	9.18	10.60	9.81	0.00	1.43	25.00	0.72
Eu	0.95	1.03	1.14	1.32	1.03	0.05	0.18	1.64	0.07
Sm	2.49	2.76	2.98	3.48	2.97	0.00	0.00	6.50	0.00
Gd	2.87	3.39	3.24	3.83	3.33	0.00	0.59	6.13	0.21
Dy	2.09	2.33	2.15	2.56	2.34	0.16	0.40	4.47	0.27
Ho	0.34	0.35	0.34	0.40	0.35	0.01	0.05	0.82	0.04
Er	0.65	0.63	0.61	0.73	0.61	0.00	0.05	1.95	0.06
Yb	0.30	0.27	0.27	0.31	0.17	0.00	0.00	1.54	0.00
Lu	0.033	0.028	0.028	0.033	0.024	0.000	0.000	0.249	0.171

Table 2 (continued)

Rock type	Green HT pyroxenite		Dark green HT pyroxenite			Black Ga megapyroxenite			
Element	315-13Cpx	315-104 Cpx	315-117 Cpx	315-116 Cpx	315-254 Cpx	315-254 ga	315-73 Cpx	315-184 Cpx	315-184 ga
Hf	1.80	2.31	3.62	3.44	2.71	0.20	0.56	2.18	0.16
Ta	0.053	0.033	0.059	0.059	0.113	0.390	0.365	0	0.293
Pb	0.10	0.16	0.16	0.13	0.00	0.00	0.00	0.00	0.00
Th	0.03	0.02	0.03	0.03	0.04	0.01	0.06	0.02	0.03
U	0.01	0.00	0.01	0.01	0.00	0.00	0.00	0.00	0.01
Sc	16.3	13.4	14.3	13.4	13.1	5.8	5.5	55.0	10.3
V	534		235	307					
Co	51.9	54.8	43.6	44.1	34.8	322.	31.5	29.3	213
Cu	13.13	12.52	10.23	14.86	6.36	22.13	31.03	4.23	14.89
Zn	52.7	64.7	57.3	63.7	35.5	57.3	37.8	35.7	20.7
Rb	0.36	0.15	0.49	0.47	0.44	707	401	0.22	580
Sr	100	112	133	156	73.0	149.9	181.0	141.4	357.3
Y	7.39	8.57	7.10	8.53	8.59	0.29	1.37	21.53	1.04
Zr	48.20	46.40	94.90	93.60	57.16	2.92	10.94	53.23	1.80
Nb	0.38	0.27	0.25	0.42	0.66	3.01	3.40	0.18	1.47
Cs	0.005	0.005	0.004	0.004	0.009	9.1	12.1	0.002	1.9

	Kaersutite Pl-pyroxenite		Kaersutite vein			Low pressure cumulate			
Element	315-249 Cpx	315-249 kaers	315–414 kaers	315-417 kaers	327-2 Cpx	327-2 Opx	327-3 Cpx	327-5 Cpx leached	327-5 Opx
SiO_2	48.45	40.42	42.61	41.05	49.03	51.85	47.05	48.99	52.12
TiO_2	1.14	5.44	4.24	5.25	1.13	0.18	1.71	0.59	0.11
Al_2O_3	7.85	14.22	12.49	14.23	6.65	4.73	9.23	8.22	6.13
Cr2O3	0.12	0.033	0.28	0.029	0.01	0.02	0.02	0.01	0.00
FeO	7.71	9.07	7.48	7.27	9.29	19.51	9.80	7.17	15.33
Mn		0.057		0.064					
MgO	11.31	13.69	14.92	14.58	11.70	23.39	9.82	12.49	26.64
CaO	20.07	9.56	9.42	9.7	20.01	0.54	20.78	21.10	0.44
Na_2O	1.94	2.98	3.27	2.99	1.59	0.06	1.31	1.42	0.05
K_2O		1.93	1.69	1.95	1.13			0.59	
Total	98.59	97.40	96.40	97.11	100.54	100.28	99.72	100.59	100.82
Ba	50.5	526	99	108	1.46	64.4	11.9	6.12	9.89
La	5.74	9.61	10.66	7.05	8.43	3.78	11.2	7.37	0.25
Ce	24.7	36.5	35.4	25.6	46.8	15.9	46.9	35.5	0.61
Pr	4.61	6.27	6.29	3.70	9.44	3.13	8.58	6.28	0.09
Nd	24.7	35.2	36.7	20.8	53.2	17.1	41.5	31.5	0.42
Eu	1.99	2.49	2.91	1.84	3.31	1.02	1.73	1.68	0.03
Sm	6.98	8.98	8.96	5.70	13.97	4.02	6.59	6.62	0.10
Gd	5.91	7.61	8.85	5.45	12.9	3.76	3.63	4.57	0.10
Dy	3.00	3.57	5.37	3.35	8.40	2.63	1.13	2.03	0.07
Ho	0.43	0.47	0.84	0.48	1.44	0.49	0.15	0.28	0.01
Er	0.78	0.92	1.68	1.04	3.46	1.19	0.26	0.55	0.03
Yb	0.37	0.45	0.86	0.60	2.65	1.09	0.13	0.30	0.03
Lu	0.05	0.06	0.136	0.07	0.367	0.169	0.02	0.039	0.005
Hf	5.37	3.59	4.10	2.95	8.56	2.55	2.60	3.69	0.31
Ta	0.01	1.23	3.50	3.90	0.066	0.17	0.10	0.081	0.29
Pb	0.31	1.66	0.08	0.47	0.44	1.12	0.31	0.53	0.19
Th	0.13	0.16	0.10	0.08	0.17	0.06	0.23	0.10	0.01
U	0.02	0.03	0.02	0.05	0.05	0.02	0.03	0.05	0.01
Sc	51.4	51.2	17.9	19.9	61.3	35.3	1.03	11.2	3.8
V							49.4		
Co	34.7	59.7	175	51.6	35.6	79	57	27.3	133
Cu	9.60	22	10.6	25.6	8.18	5.97	11.0	1.87	2.05
Zn	41.4	56.7	37.9	48.4	80.3	226	127	15.5	92.7
Rb	0.84	9.23	6.67	0.49	0.55	1.53	0.604	0.07	0.37
Sr	182.	706.	599	678	51.4	106.0	84.9	104.	16.4
Y	13.5	15.3	19.6	11.32	28.80	12.6	3.36	5.24	0.36
Zr	193.	133	114	90.	238.	85.	120.	91.2	8.58
Nb	0.43	8.36	51.6	54.3	0.96	2.31	1.05	0.05	0.35
Cs	0.01	0.01	0.037	0.00	0.001	0.012	0	0.003	0.007

	Cr–Di websterites								
Element	315-251 Cpx	315-252 Cpx	315-252 ga	315-252 Opx	315-253ga	315-253Cpx	315-124 Cpx	315-124 ga	324-3 Cpx	324-3 ga
SiO_2	51.79	51.87	42.35	54.26	42.32	52.11	52.42	41.71	52.03	41.77
TiO_2	0.28	0.37	0.18	0.14	0.23	0.54	0.80	0.24	0.60	0.20
Al_2O_3	6.47	5.99	23.13	4.07	22.71	6.31	6.23	22.92	6.19	22.88
Cr2O3	0.80	0.29	0.34	0.17	0.79	0.405	0.13	0.14	0.61	0.88
FeO	3.32	3.47	7.84	6.57	7.90	3.32	3.92	10.31	2.99	7.34
Mn						0.085				
MgO	16.00	16.12	20.90	32.79	20.84	15.74	15.01	18.12	15.49	22.08

Table 2 (*continued*)

	Cr–Di websterites									
Element	315-251 Cpx	315-252 Cpx	315-252 ga	315-252 Opx	315-253ga	315-253Cpx	315-124 Cpx	315-124 ga	324-3 Cpx	324-3 ga
CaO	18.40	18.52	4.97	0.94	4.96	18.14	18.06	6.07	18.75	5.12
Na$_2$O	1.95	2.01	0.03	0.20	0.09	2.34	1.97	0.04	1.84	0.06
K$_2$O	0.28	0.37		0.01						
Total	99.29	99.01	99.74	99.15	99.84	98.99	98.54	99.55	98.50	100.33
Ba	1.00	0.26	0.34	12.97	0.23	4.49	2.22	0.17	1.52	0.17
La	1.41	1.94	0.03	0.37	0.02	1.23	2.23	0.03	2.13	0.03
Ce	4.58	6.89	0.10	1.28	0.14	4.15	7.31	0.13	6.72	0.09
Pr	0.82	1.14	0.05	0.25	0.05	0.819	1.59	0.06	1.37	0.03
Nd	4.18	6.24	0.37	1.47	0.56	4.72	8.49	0.69	7.02	0.40
Eu	0.47	0.74	0.39	0.13	0.64	0.68	0.97	0.46	0.76	0.42
Sm	1.21	1.99	0.59	0.46	0.89	1.73	2.82	0.80	2.23	0.68
Gd	1.39	2.36	2.14	0.60	3.50	2.16	2.99	2.34	2.36	2.31
Dy	1.12	1.55	5.36	0.64	8.88	1.62	2.07	4.72	1.55	4.82
Ho	0.21	0.23	1.42	0.13	2.36	0.271	0.32	1.18	0.23	1.22
Er	0.48	0.46	4.47	0.37	7.49	0.55	0.63	3.80	0.45	3.90
Yb	0.33	0.23	4.97	0.39	7.71	0.303	0.32	4.18	0.22	4.24
Lu	0.046	0.025	0.863	0.061	1.11	0.037	0.04	0.65	0.03	0.65
Hf	0.43	0.83	0.44	0.51	0.67	0.865	6.56	0.70	1.18	0.80
Ta	0.027	0.103	0.050	0.148	0.001	0.02	0.53	0.09	0.31	0.00
Pb	0.17	0.10	0.00	0.44	0.00	0.30	0.04	0.001	0.09	−0.11
Th	0.04	0.13	0.01	0.02	0.00	0.04	0.13	0.00	0.12	0.00
U	0.01	0.03	0.00	0.02	0.00	0.02	0.03	0.01	0.03	0.01
Sc	22.1	28.5	31.4	9.5	27.6	0.32	30.7	89.4	22.8	83.4
V	294		108			30.8				
Co	29.3	12.7	29.4	111	30.9	510	27.5	54.	25.3	44.4
Cu	8.71	3.79	0.68	4.56	0.92	24.3	6.55	2.38	4.83	1.35
Zn	15.2	7.2	7.0	424	8.3	9.61	17.6	15.4	13.7	11.6
Rb	0.07	0.00	0.23	0.64	0.11	1.15	0.04	0.05	0.02	0.06
Sr	95	88	1.4	13.0	0.3	0.16	108	0.70	100	0.27
Y	4.75	4.58	29.2	3.91	41.7	91	9.85	40.7	7.33	41.3
Zr	13.1	21.1	23.2	15.9	42.9	6.12	196	46.9	38.4	34.7
Nb	0.34	0.39	0.32	0.36	0.02	28.8	1.47	0.24	1.35	0.12
Cs	0.002	0.002	0.001	0.009	<0.01	0.01	0.01	0.01	0.001	0.00

	Gray Cr-low Ga Cpxt					Sp lherzolite, v.Kandi dushka	Ga-Phl lherzolites			
Element	315-110Cpx	315-110ga*	315-305Cpx	315-305ga	315-302Cpx	302-202cp	313–703Cpx	313-703ga	313-878Cpx	315-878ga
SiO$_2$	50.97	41.9	51.43	41.93	51.94	51.68	52.10	41.96	51.96	42.31
TiO$_2$	0.47	0.13	0.71	0.22	0.72	0.81	0.61	0.164	0.74	0.21
Al$_2$O$_3$	7.71	22.95	6.97	23.12	7.04	7.48	5.99	22.63	6.71	22.44
Cr2O3	0.11	0.1	0.13	0.10	0.13	0.91	1.14	1.06	0.99	1.32
FeO	3.63	9.44	4.67	10.61	4.72	4.07	3.47	7.9	3.81	7.12
Mn						0.10	0.81	0.323		
MgO	14.03	18.59	14.62	17.46	14.77	14.90	15.52	20.55	15.80	20.84
CaO	18.69	6.45	18.44	6.68	18.62	16.32	18.16	4.68	16.76	5.10
Na$_2$O	2.14	0.09	2.04	0.04	2.06	2.58	1.61	0.03	2.37	0.03
K$_2$O	0.47		0.71	0.00						
Total	98.22	99.65	99.71	100.17	100.00	98.85	99.41	99.30	99.13	99.37
Ba	0.77	0.93	1.41	0.20	5.20	1.26	1.12	0.28	3.21	7.25
La	1.51	0.03	1.96	0.02	1.87	4.15	1.46	0.02	1.73	0.04
Ce	5.05	0.15	4.64	0.13	6.20	15.1	5.53	0.15	5.26	0.09
Pr	0.85	0.06	0.68	0.04	1.09	2.47	1.11	0.05	0.96	0.04
Nd	4.61	0.51	3.50	0.46	5.90	13.21	6.69	0.58	5.80	0.22
Eu	0.51	0.38	0.45	0.59	0.56	1.40	0.86	0.60	0.62	0.45
Sm	1.31	0.58	1.23	0.94	1.56	3.87	2.32	0.87	1.79	0.66
Gd	1.25	1.57	1.71	3.94	1.64	4.50	2.69	2.96	2.01	2.51
Dy	0.72	2.87	1.15	8.28	0.91	3.36	1.86	6.93	1.31	6.13
Ho	0.10	0.75	0.17	2.00	0.14	0.56	0.28	1.80	0.19	1.64
Er	0.19	2.25	0.32	6.08	0.25	1.25	0.56	5.41	0.36	5.03
Yb	0.09	2.20	0.18	5.83	0.14	0.82	0.31	5.14	0.17	5.62
Lu	0.010	0.39	0.021	0.844	0.017	0.105	0.038	0.708	0.025	0.982
Hf	0.57	0.33	0.60	0.47	0.83	1.81	1.74	0.57	1.04	0.58
Ta	0.205	0.05	0.248	0.217	0.259	0.267	0.119	0.001	0.037	0.083
W	0.11	0.20	0.23	0.19	0.07	0.21	0.05	0.04	0.03	0.08
Pb	0.15	0.03	0.21	0.00	0.08	0.15	0.15	0.01	0.11	0.00
Th	0.19	0.00	0.14	0.01	0.09	0.26	0.10	0.00	0.09	0.02
U	0.06	0.01	0.04	0.01	0.02	0.06	0.02	0.00	0.01	0.00
Sc	13.5	60.7	23.7	51.2	16.0	47.6	31.6	34.9	25.0	85.8
V										
Co	34.0	71.5	34.5	43.0	34.9	24.2	24.5	29.3	299	121.1
Cu	13.04	2.77	10.8	5.45	7.17	6.41	6.83	0.71	3.72	0.82

Table 2 (continued)

| Element | Cr–Di websterites | | | | | | | | | |
	315-251 Cpx	315-252 Cpx	315-252 ga	315-252 Opx	315-253ga	315-253Cpx	315-124 Cpx	315-124 ga	324-3 Cpx	324-3 ga
Zn	21.5	16.4	23.2	18.1	21.7	17.4	17.0	10.7	8.4	7.2
Rb	0.17	3.16	0.10	0.02	0.20	0.07	0.02	0.23	0.30	1.41
Sr	52.4	0.60	67.5	26.5	86.2	159	78.9	0.4	65.6	1.0
Y	4.41	23.3	4.18	24.4	3.24	5.47	5.37	31.0	4.99	39.8
Zr	8.21	17.8	10.03	9.38	21.58	95.9	51.9	41.5	25.1	35.9
Nb	1.22	0.45	1.51	0.18	1.12	1.99	0.71	0.05	0.58	0.22

	Glasses from Gl 7	Picrite Gl 8	Basalts Gl9
Ba	4763	2264	3501
La	90.	78	84
Ce	229	191	207
Pr	22.6	19.5	22.1
Nd	91	78	82
Eu	15.2	13.4	15.4
Sm	5.17	4.73	5.10
Gd	11.9	7.96	12.2
Dy	6.92	6.11	6.11
Ho	0.98	1.042	0.82
Er	2.10	1.89	2.15
Yb	1.67	1.27	1.43
Lu	0.24	0.159	0.177
Hf	5.37	4.999	5.54
Ta	4.51	4.33	4.27
W	0.196	0.33	0.140
Pb	20.53	34.73	23.42
Th	9.22	7.90	8.17
U	1.60	1.49	1.83
Sc	23.61	21.2	24.83
Ti	27,672	24,103	27,922
Co	57	50	49.3
Cu	399	574	357
Zn	319	490	489
Rb	76.	93.3	97.8
Sr	4007	1976	3188
Zr	297.	292.	271
Nb	101	112	115
Mo	0.429	0.644	0.640
Cr	220	181	1024
V	442	365	447
Ni	1217	1747	1149

Note: Major components are determined by EPMA on CamebaxMicro in Analytic Center, UIGGM, analyst Khmelnikova OS.
Trace elements – for minerals were determined in the Royal Museum Central Africa, Tervuren, by solutions LICP MS in Belgium, analyst L. Andre . The compositions of trace elements for glasses from picrite basalts were made by laser ablation (see analytical methods).

Table 3
Isotopic ratios determined for selected minerals from Vitim pyroxenite xenoliths.

Sample	87Sr /86Sr	143Nd/144Nd	ε Nd
Garnet black megacrystalline pyroxenite 315–254 Cpx1	0.704077 ± 0.000040	0.512881 ± 0.000005	+4.74
Garnet black megacrystalline pyroxenite 315–254 Cpx2	0.703913 ± 0.000030	0.512899 ± 0.000007	+5.09
Cr-diopside garnet wbsterite 315-252 Cpx	0.703095 ± 0.000020	0.513033 ± 0.000005	+7.70
Transitional garnet websterite 315–110 Cpx	0.703019 ± 0.000040	0.513106 ± 0.000008	+9.12
Plagioclase websterite 315-108 Cpx	0.710607 ± 0.000060	0.512179 ± 0.000004	−8.95
Plagioclase websterite (cumulate) 327–2 Cpx	0.705245 ± 0.000020	0.512465 ± 0.000006	−3.37

Determined in Institute of Precambrian Geology and Geochronology RAS, St. Petersburg, on multi-collector mass-spectrometer FinniganMAT-261 in static mode. The $^{143}Nd/^{144}Nd$ ratio was normalized within-run to $^{148}Nd/^{144}Nd = 0.241570$ and then adjusted to a $^{143}Nd/^{144}Nd$ value of 0.511860 for La Jolla. Sr isotope composition was normalized within-run to $^{88}Sr/^{86}Sr = 8.37521$. The value of Sr isotope standard SRM-987 during this work was $^{87}Sr/^{86}Sr = 0.710248 ± 15$ (2σ, 6 runs). Assigned errors (2σ) for $^{147}Sm/^{144}Nd$ and $^{143}Nd/^{144}Nd$ were ± 0.3% and ±0.000015, $^{87}Rb/^{86}Sr ± 0.5\%$, $^{87}Sr/^{86}Sr ± 0.000025$ according to results of multiple analyses of standard (external reproducibility). The 2σ errors cited in table for $^{143}Nd/^{144}Nd$ and $^{87}Sr/^{86}Sr$ reflect in-run precision and demonstrate only quality of these analyses. The blank level for Sm was 0.01 ng and 0.05 ng for Nd, 0.05 ng for Rb and 0.2 ng for Sr. The data obtained for BCR-1 during course of this analytical work are: [Sr] = 335.8 ppm, [Rb] = 47.16 ppm, [Sm] = 6.487 ppm, [Nd] = 28.45 ppm, $^{87}Sr/^{86}Sr = 0.705053 ± 11$, $^{87}Rb/^{86}Sr = 0.40615$, $^{143}Nd/^{144}Nd = 0.512663 ± 9$, $^{147}Sm/^{144}Nd = 0.13829$ and data for Sr standard SRM-987 were $^{87}Sr/^{86}Sr = 0.710248 ± 15$ (2σ, 6 runs), and for Nd standard La Jolla – $^{143}Nd/^{144}Nd = 0.511869 ± 12$ (2σ, 5 runs).

with differing *Fe#* values (group IId, Litasov et al., 2000), increasing in general from veins cutting garnet lherzolites to those cutting spinel lherzolites.

Clinopyroxenes plagioclase-bearing LPC or group III (Litasov et al., 2000) deviate from the trend towards lower Na₂O and Al₂O₃ values. Three separate groups of clinopyroxenes with similar FeO contents forming ascending trends of Na₂O, Al₂O₃ and TiO₂, and clusters near 8, 10 and 11 wt.% FeO relate to the three separate subgroups of black pyroxenites. The most Fe-rich clinopyroxenes (LPC) continue the megacrystalline trend.
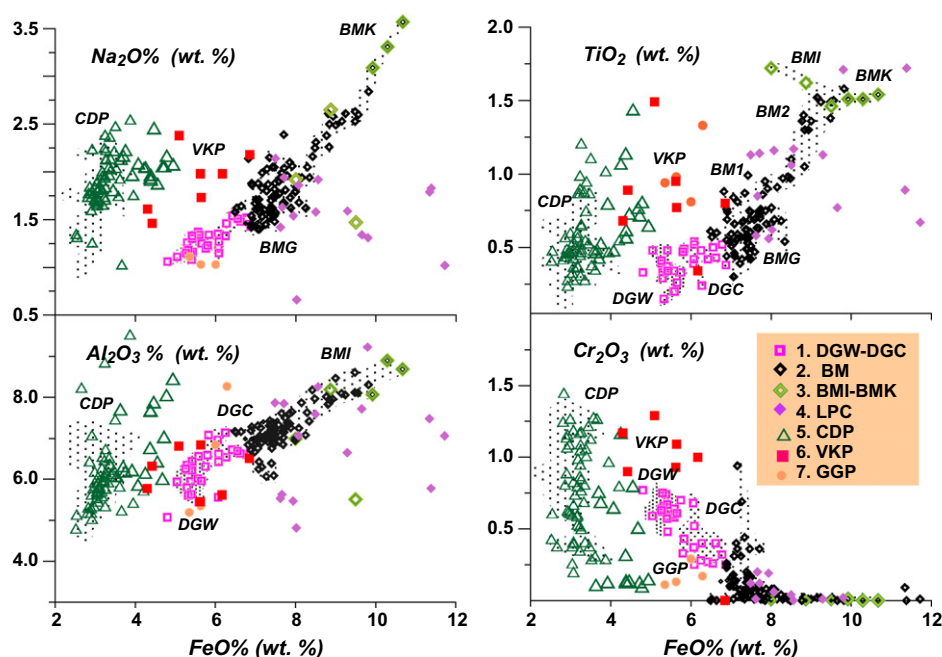
Fig. 3. Variation diagram for pyroxenites found as inclusions in Vitim picrite-basalts. (1) Dark green Cr-bearing pyroxenites (DGW-DGC). (2) Black garnet-bearing coarse-grained pyroxenites (BMP). (3) The same but ilmenite–phlogopite-bearing (BMI-BMK). (4) Plagioclase-bearing fine-grained low pressure cumulates (LPC); (5) Green Cr-diopside websterites (CDP). (6) Veined and composite pyroxenites and peridotites (VAPP). (7) Gray garnet pyroxenites (GGP). The shaded area in the left low-Fe part corresponds to the lherzolites. (For interpretation of the references to colour in this figure legend, the reader is referred to the web version of this article.)

Clinopyroxenes in Cr-diopside pyroxenite veins (CDP) (group I of Litasov et al., 2000) are very similar in composition to those from the lherzolites (2.7–3.5 wt.% FeO), although they are slightly more enriched in 'basaltic' components (FeO, TiO_2, Na_2O, Al_2O_3).

Compared with the earlier study of Ashchepkov et al. (1994), pyroxenite xenoliths studied here has yielded similar distributions of petrographic groups and clinopyroxene trends.

6. Thermobarometry

P-T diagram that covers all of the observed lithologies may be obtained with the monomineral barometry for clinopyroxenes. We have used the method of Nimis and Taylor (2000) for temperatures showing good agreement with the experimental values (Taylor, 1998; Walter, 1998; Yaxley, 2000; Dasgupta et al., 2007; Brey et al., 2008; Foley et al., 2009; etc.) (Fig. 4a) giving similar estimates as Brey and Kohler (1990) two pyroxene thermometer (Fig. 4c). Modified versions of a Jd-Di clinopyroxene barometer (Ashchepkov, 2002; Ashchepkov et al., 2010) after introduction in the KD of corrections for the temperature for Al, Ti, Fe achieved better agreement with the experimental data and calculations made using Nimis and Taylor (2000) barometer (Fig. 4b,d) (supplemental file 3). This version is applicable to the augite and Cr-diopside Na–Al clinopyroxenes typical for peridotite and pyroxenite xenoliths from alkali basalts as well as for the low-Al clinopyroxenes from kimberlite xenoliths.

PT estimates of Brey and Kohler (1990) obtained for the comparison (Fig. 5a) produces for the green xenolith suite, including lherzolites and the CDP group, a hot geotherm with a geothermal gradient close to 90 mw/m², typical for convective geotherm determined for the xenoliths from alkali basalts from SE Australia (O'Reilly and Griffin, 1985) and other localities from the various geodynamic environments (e.g. Nixon and Boyd, 1979; Ashchepkov et al., 1996; Stern et al., 1999; Mukhopadyay and Manton, 1994; Lee et al., 2001; Xia et al., 2004; Ionov, 2007; Su et al., 2009). The method of Brey and Kohler (1990) yields estimates that form a high temperature branch between 2.7 and 2.5 GPa for the

typical black garnet pyroxenite series and, additionally, a cluster located close to the lherzolitic field near 1.5–1.6 GPa (Fig. 5a), coinciding with the location of the low temperature CDP group. The PT estimates for LPC xenoliths with values ⩽1.2 GPa show deviations from the geotherm to low temperature conditions.

A more detailed PT diagram (Fig. 5b) produced by monomineral clinopyroxene thermobarometry (Ashchepkov et al., 2010) demonstrate good agreement with the results obtained using polymineralic thermobarometry (Fig. 5a) (supplemental file 4) for orthopyroxene – bearing pyroxenites. The PT values for the green pyroxenite CDP and lherzolites xenoliths plot near the SE Australian convective geotherm (O'Reilly and Griffin, 1985) (Fig. 5b) deviating to colder conditions. Websterites are determined near 1.7–2.3 GPa, and together with the orthopyroxenites at the base – 2.9–2.7 GPa while the middle part is correspondent mainly to the garnet wehrlites. The VVP locating between the PT arrays for the BM and CDP are associated with surrounding metasomatic peridotites with hydrous minerals. They reveal some clustering in PT diagram. Phlogopite-bearing orthopyroxenites prevail in the deeper part of the mantle section at 2.8–2.5 GPa. Kaersutite-bearing veins in garnet lherzolites yield pressures of 2.5–2.3 GPa. Intergranular pargasites in garnet lherzolites (Glaser et al., 1999) commonly appear at 2.5–2.0 GPa, although in the shallow mantle Ti-pargasites are common in SL at 1.2–1.5 GPa, sometimes surrounding monomineralic kaersutite veins. The GGP rocks that are sometimes found at the contacts of the VAPP and BM associations give a pressure range of 1.7–2.2 GPa.

PT points for GL show variations from 2.7 to 1.7 GPa near SEAG with the deviations to hot geotherm produced by BM suit. The smaller range based on restricted analyses (Ionov et al., 1993, 2005; Glaser et al., 1999) including amphibole and phlogopite bearing peridotites determine the gently inclined line in middle part of PT array for lherzolites in the range of 1.7–2.4 GPa.

The black Al–Ti–augite suite produces a stepped PT range which is less stepper in general then determined by Litasov et al. (2000) who used unequilibrated assemblages with Cr-bearing clinopyroxenes and Cr-free garnets. The highest temperature points for the Al-augite group fall into the six intervals from 3.3 to 1.1 GPa,
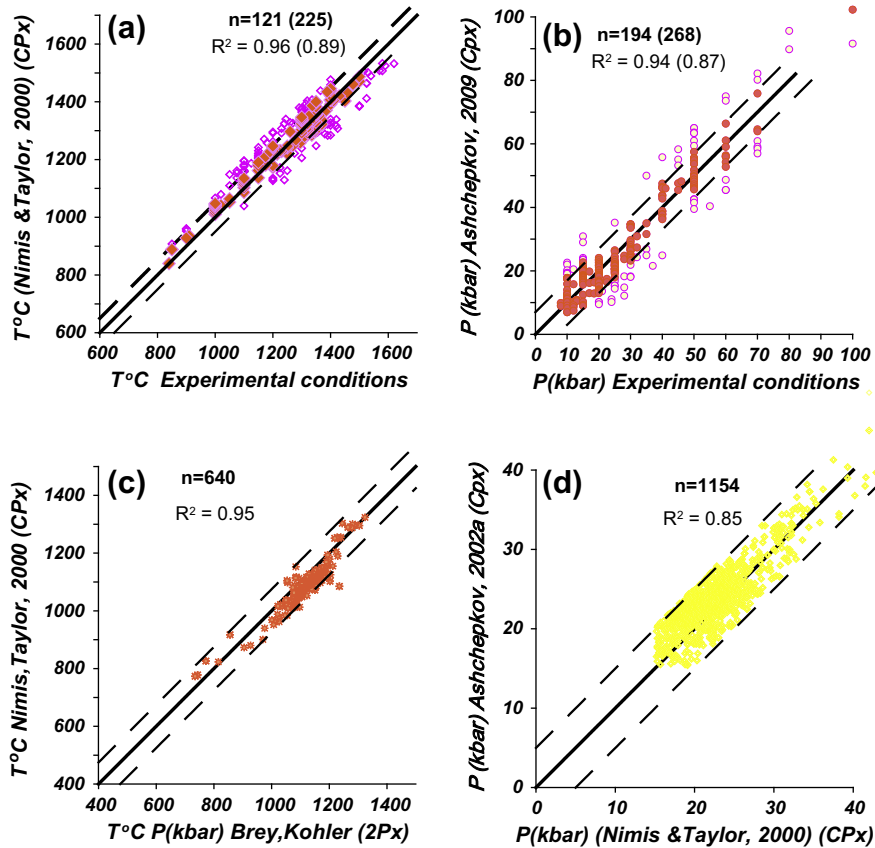
Fig. 4. Correlations: (a) between temperatures of the experimental runs and values estimated with monomineral thermometer (Nimis and Taylor, 2000) for the clinopyroxenes, the solid circles are for data used for calibration in this work (Nimis and Taylor, 2000): (Taylor, 1998; Walter, 1998; Brey and Kohler, 1990; and in addition from Brey et al., 2008), the open circles are for the extended data set (Foley et al., 2009; Walter, 1998 and references therein); (b) between the pressures of the experimental runs and values estimated with monomineral thermometer (Ashchepkov et al., 2011 (Ashchepkov et al., 2010 modified) (see Appendix A); the solid and open circles mean the same as above; The correlations of the temperatures (c) and pressures (d) obtained for the Vitim (Ashchepkov and Andre, 2002; Litasov et al., 2000) and worldwide pyroxenites (Frey, 1980; Pearson and Nowell, 2004; Upton et al., 2003; Downes, 2007; Zheng et al., 2009) using polymineral thermobarometry (Brey and Kohler, 1990) (see Appendix A equation set 1) and monomineral methods (Nimis and Taylor, 2000) for temperatures and Ashchepkov et al. (2010) (modified) for pressures.
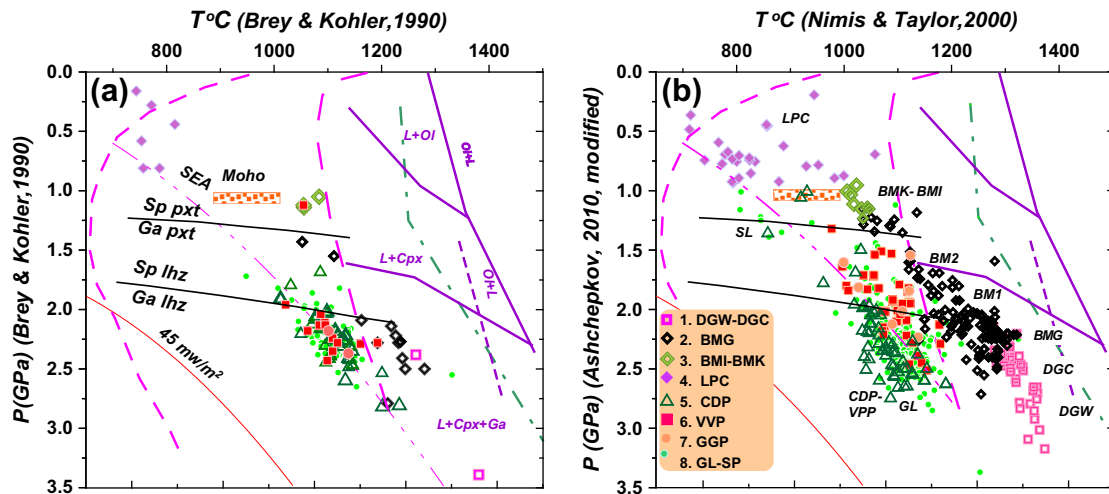
Fig. 5. Pressure-temperature diagrams for mantle xenoliths from Vitim picrite basalts obtained using: (a) Brey and Kohler, (1990) methods; (B) Nimis and Taylor (2000) thermometer and Ashchepkov (2002) barometer (symbols are as in Fig. 3). Phase boundaries for primitive alkali basalts according to modeling from Rankenburg et al. (2004) are given by the lines, liquidus lines for basanites (Arculus, 1975; Esin et al., 1993) by dot-and-dash lines; the liquidus and solidus for Ne-mugearites are after Irving and Green (2008) are drown by dashed lines, Symbols are the same as in Fig. 3. (For interpretation of the references to colour in this figure legend, the reader is referred to the web version of this article.)

creating the lower part of a sub-adiabatic *P–T* path which is continued by several points up to 1.2 GPa. The estimates for hybrid DGW – DGC series for BM suit form two clusters from 3.2 to

2.5 GPa. The typical BMG clinopyroxenes give two arrays of cooling from 1300 to 1200 °C around 2.2 and 2.5 GPa. An inclined PT path continues the trend derived from this cloud, forming two additional
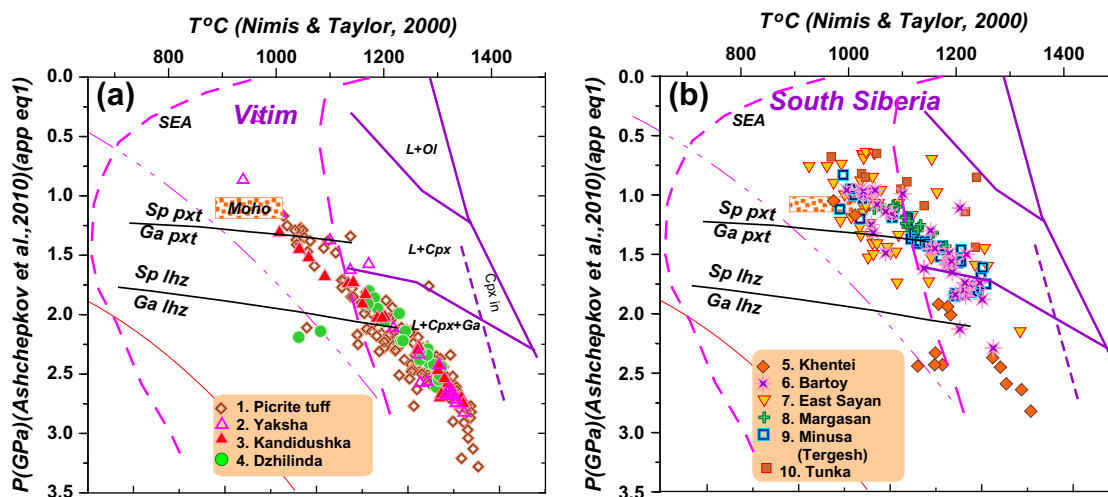
Fig. 6. Pressure-temperature diagram for Vitim megacrystalline pyroxenite xenoliths and megacrysts based on Nimis and Taylor (2000) thermometer and Ashchepkov (2002) barometer. Data from Ashchepkov et al. (2003). (1) Miocene picrite-basalt black suite (BM–DGW–DGC); (2) BM from Pleistocene Yaksha volcano; (3). BM from Pleistocene Kandidushka Quaternary volcano; (4) BM from Pliocene Dzhilinda lava flow; (5) Burkal (Zharnichikha) river Khentei ridge (N 49.674, E 109.785) (Ashchepkov et al., 1996); (6) Southern Khamar-Daban (Dzhida) Bartoy volcanoes (N 50.723, E 103.297) (Ashchepkov, 1991); (7) Northern Khamar-Daban, Miocene Margasan river flow (N 51.621, E 102.940) (near rift valley); (8) Minusa Tergesh volcano BM series (Ashchepkov et al., 1995a); (9) Tunka valley, neck near Pliocene volcano Kavrizhka (N 51.849, E 102.512) (Ashchepkov, 1991); (10) Tuva megacrysts from Eastern Sayan Pleistocene lavas (Rasskazov et al., 2002).

sub-groups for BM1 (~2.2–2.0 GPa) and BM2 (~1.5–1.8 GPa) with the subtrends of nearly isobaric cooling to the SEA geotherm continued by the VVP points. The continuation of cooling range to the garnet –spinel transition corresponds to the BMI –BMK groups giving scattered cloud of PT points at ~1.5–1.2 GPa, near the Moho boundary. The LPC plagioclase-bearing cumulates show two lines of decreasing PT conditions at the pressure range from 0.3 to 1.2 GPa and temperatures from 700 to 1110 °C.

Comparison of Pt estimates for megacrysts from the three main stages of volcanic activity in Vitim, corresponding to the middle Miocene (~14 Ma picrite-basalts), the Pleistocene lava flows (ca 2–1.5 Ma basanites and Ne-hawaiites) and the final cinder cone eruptions (~0.8 Ma Ne-hawaiites and mugearites at Kandidushka and Yaksha volcanoes)(Ashchepkov et al., 2003) (Fig. 6a) and several localities of megacrysts in xenolith-bearing basalts in Trans Baikal and Southern Siberia (Ashchepkov, 1991; Ashchepkov et al., 1996, 2003; Rasskazov et al., 2002) (Fig. 6b) reveal a good agreement with the pressure range of the xenoliths (Ashchepkov et al., 2003) and BM suits.

7. Trace elements

Trace elements for BM clinopyroxenes and some garnet, mica, amphibole and orthopyroxene separates were determined for 2–3 representative samples from most of pyroxenite groups. Clinopyroxenes from the BM suite reveal a sequential increase in incompatible element content and simultaneous decrease of HREE (Fig. 7). Multi-element spidergrams of BM clinopyroxenes are less inflected than those of clinopyroxenes from the green CDP, lherzolitic and GGP series. The data set of 16 analyses obtained by SIMS (Litasov et al., 2000) for a more restricted range of elements show good agreement with our analyses (Andre and Ashchepkov, 1996; Ashchepkov and Andre, 2002). Combined with the trace element patterns for ilmenite-bearing high temperature associations and data from Andre and Ashchepkov (1996) and Litasov et al. (2000), this work reflects the variation of the trace elements for the whole pyroxenite suite.

The shape of the REE patterns and inclination of their REE slopes (La/Sm$_n$ and Gd/Yb$_n$ ratios) suggest 1% melting of parent magma

from a primitive source (McDonough and Sun, 1995) similar to common CDP and lherzolitic clinopyroxenes (see supplemental file 5). From the BMG to BMK groups, the incompatible element concentrations (LREE, Th, U, Ta, Nb and LILE) in the clinopyroxenes increase. This is more evident for Rb, Ba, whereas the other LILE reveal more complex behavior possibly influenced by fluids (Stalder et al., 1998). The high concentrations of Ba and LREE in tiny fluid inclusions were detected by an autoradiographic method (Dobretsov et al., 1992) and by leaching experiments by Andre and Ashchepkov (1996). LILE content is higher in clinopyroxenes from hydrous veins, while Ta and Nb are often lower due to coeval crystallization of kaersutite and oxides (Ionov and Hofmann, 1995). Ta, Nb and other HFSE contents in the clinopyroxenes from the BM group are lower than in those from the lherzolites, CDP and DGW. Clinopyroxenes from GGP are more enriched in these elements as well as in U and Th.

Trace element spidergrams of the DGW and DGC clinopyroxenes are flatter and show a trough at Ta, whereas the primitive black clinopyroxenes (e.g. sample 315-154) at the boundary between the DGW and BM series (Fig. 3) reveal lower LREE contents and more rounded REE patterns.

Clinopyroxenes from CDP xenoliths are more variable in La/Nd$_n$ and Gd/Yb$_n$ ratios. They demonstrate Zr–Hf–Ti troughs whereas clinopyroxenes from the GL display only a small Zr dip (Fig. 8). Clinopyroxenes from mica- and amphibole-rich veins (VAPP) are strongly enriched LILE and LREE, but show depletion in Nb and Ta that entered the coexisting amphiboles and minor ilmenite.

Clinopyroxenes in LPC xenoliths show higher MREE concentration than those from BM groups, inclined and humped trace element patterns with troughs at Eu, Ti, Sr, Pb and Nb, low Cs and Rb concentrations, and peaks in Ba and U. Very often clinopyroxene in typical granulite xenoliths show lower concentrations of trace elements (Zheng et al., 2009).

GGP clinopyroxenes differ from the others by higher HFSE and higher (Sm/Yb)$_n$ ratios, their REE patterns which are inflected in MREE, sometimes showing a concave downward or flat REE pattern from La to Gd which is typical for phlogopites (Litasov et al., 2000 Ashchepkov and Andre, 2002).

Garnets from all samples show rounded REE patterns with high HREE contents (Fig. 9). (La/Yb)$_n$ ratios are higher for GGP, CDP and
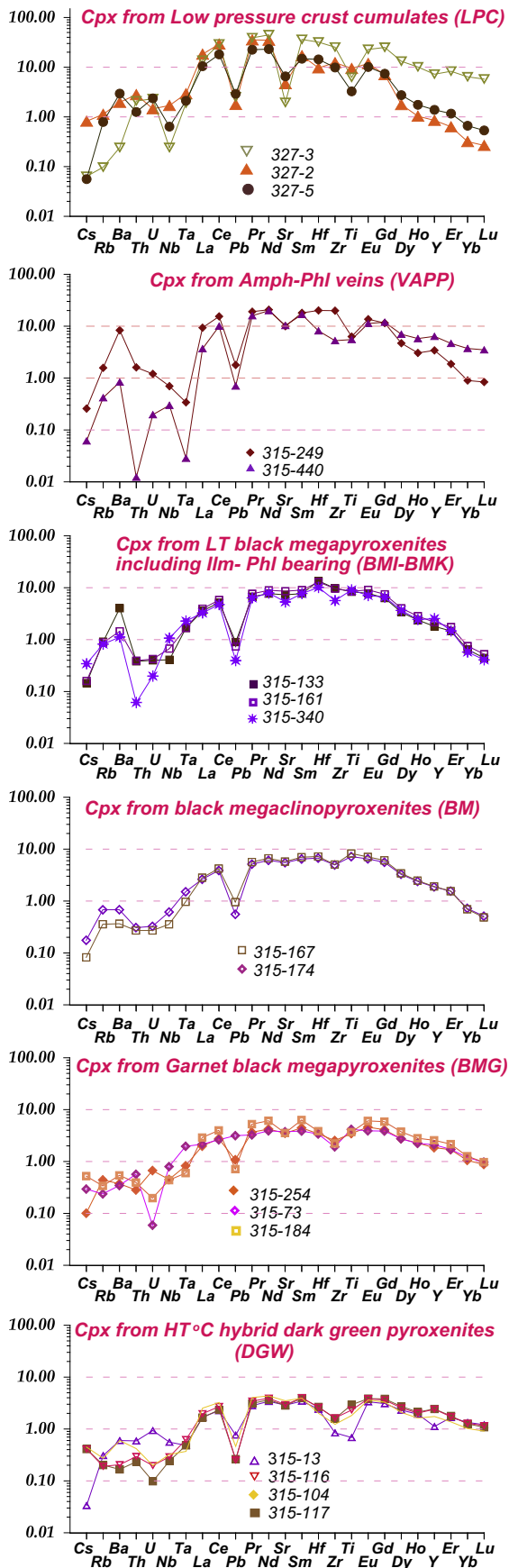
Fig. 7. Primitive mantle-normalized spidergrams for clinopyroxenes from BM xenoliths from Vitim picrite basalts normalized to values of McDonough and Sun (1995).
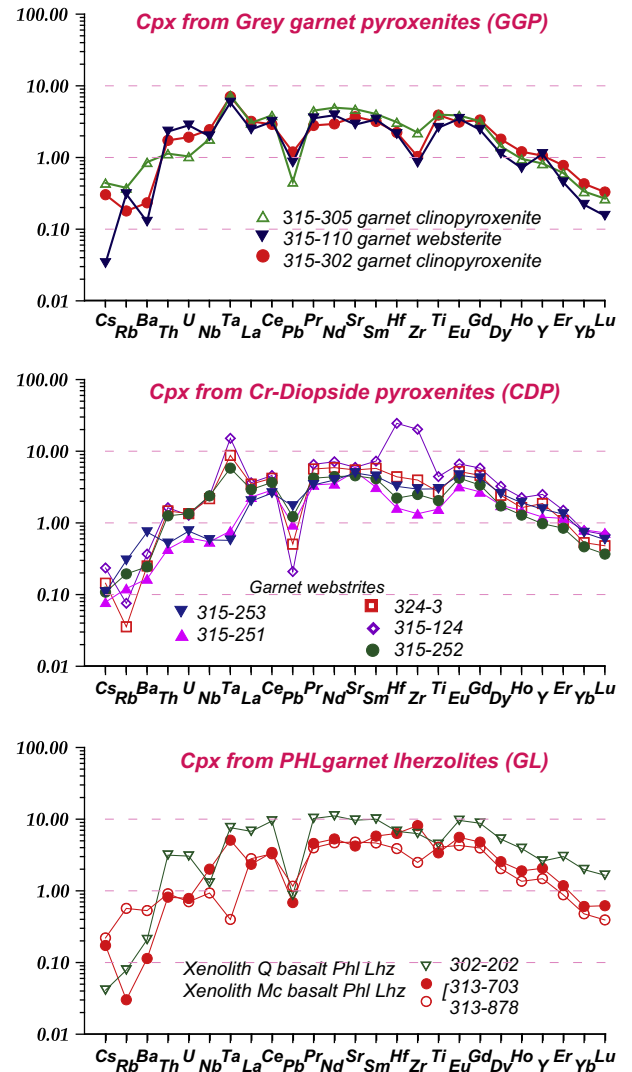

Fig. 8. Primitive mantle-normalized spidergrams for clinopyroxenes from green pyroxenite, transitional pyroxenite and lherzolite xenoliths from Vitim picrite basalts normalized to values of McDonough and Sun (1995).

lherzolite garnets and lower for BMG ones, due to lower KD for REE for high temperature garnets (Harte and Kirkley, 1997). Only rare garnets from GGP reveal a small hump in Dy. All garnet spidergrams reveal strong minima at Sr and Th. Relative enrichment in Ta, Nb, Pb and sometimes U, Rb, Ba may be explained by tiny sulfide, ilmenite and fluid inclusions because partition coefficients for these elements are low (Harte and Kirkley, 1997; Fulmer et al., 2010).

Kaersutite patterns have higher REE contents (Fig. 9) than coexisting clinopyroxenes; they have peaks in Nb and Ta, similar to those found for amphiboles in lherzolite xenoliths from Vitim and Bartoy (Ionov et al., 1992; Ionov and Hofmann, 1995; Glaser et al., 1999) and other World localities (Chazot et al., 1995; Kovács et al., 2004) regulated by their partition coefficients with the melt (Chazot et al., 1995; La Tourrette et al., 1995; Brenan et al., 1996; Dalpé and Baker, 2000; Adam and Green, 2006). Coexisting clinopyroxenes are depleted in Nb and Ta. REE distribution of micas (Fig. 9) from the BMP display flattened or inflected M-type patterns. The gentle depressions from La to Gd parts of spidergrams for samples 315-341-315-340 are similar to those of clinopyroxenes from GGP for samples 315-302 and 315-305. They demonstrate strong peaks for LILE and Pb which is in accord with the
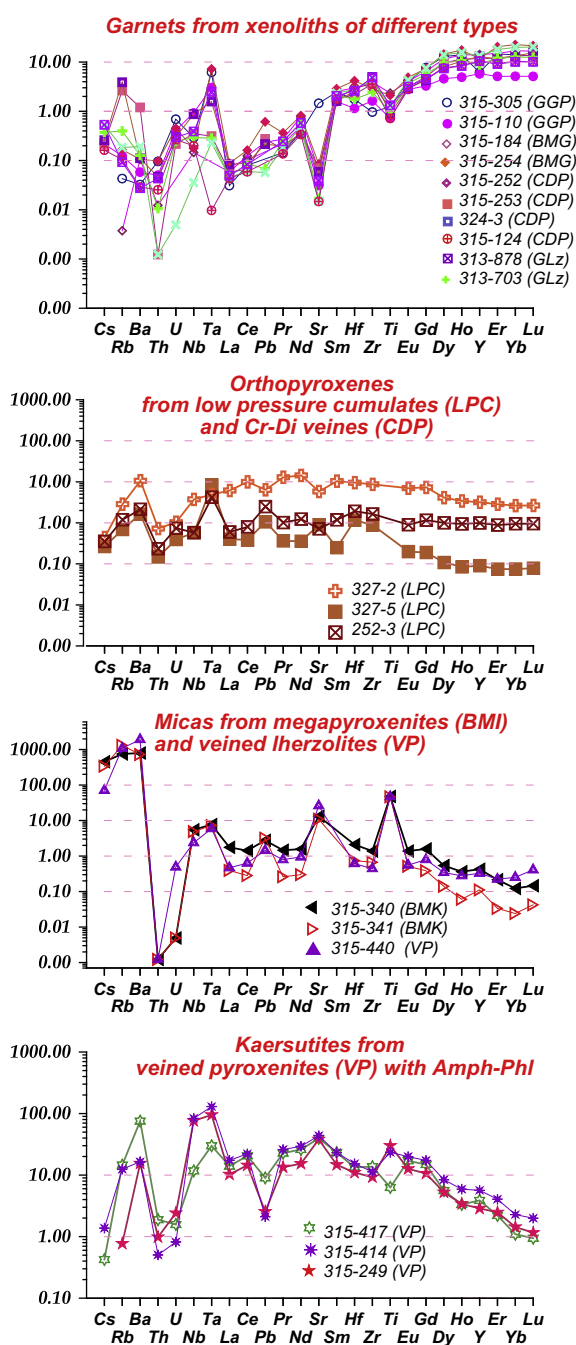
Fig. 9. Primitive mantle-normalized spidergrams for amphiboles, phlogopites, garnets and orthopyroxenes from different groups of mantle inclusions normalized to values of McDonough and Sun (1995).

presence of phlogopite (Rosenbaum, 1992), smaller ones for Nb, Ta and Sr, and very low Th-U concentrations (Foley et al., 1996). The micas in the BM pyroxenites and GL are not completely equilibrated with the clinopyroxenes as is evident from the concave-downward MREE patterns. Orthopyroxenes from the CDP have humped but gentle REE pattern near chondrite-level. In the LPC they are inclined with a very slight negative Eu anomaly.

8. Isotopic features of clinopyroxenes

The $^{87}Sr/^{86}Sr$ and $^{143}Nd/^{144}Nd$ ratios determined for clinopyroxenes from BMP (Table 3; Fig. 10) fall between the compositions of typical primitive Vitim picrite-basalts and basanites (Johnson et al.,

2005), which are close to Bulk Earth, and the field of local peridotite xenoliths (Ionov et al., 2005a,b). Data for the BM clinopyroxenites are shifted up from the mantle array along the Nd axis, suggesting contamination of their parental magma by garnet lherzolites. In shallow mantle domains where spinel lherzolites predominate, the BM minerals usually show higher Sr-isotope ratios than the host basalts (Akinin et al., 2005; Choi et al., 2008). In contrast, mica-bearing pyroxenites (Ionov and Hofmann, 1995; Ionov et al., 2005a,b) plotting on mixing line with phlogopite are displaced to lower $^{143}Nd/^{144}Nd$ values from the mantle array Garnet CDP and GGP reveal more radiogenic features than garnet peridotites, as seen in some orogenic massifs (Pearson and Nowell, 2004). The latter have lower $^{87}Sr/^{86}Sr$ and higher $^{143}Nd/^{144}Nd$ ratios.

9. Discussion

9.1. Models of origin for different pyroxenite groups

Typical magmatic signatures of Vitim pyroxenite xenoliths are demonstrated by the variations in trace and major elements in the clinopyroxenes, suggesting different and possibly multistage origins. In the models of fractionation and/or mixing of the BM suite, we take sample 315-254 as the least contaminated end-member. Data for this pyroxenite are located at the boundary between DGW and BMG in the clinopyroxene variation diagrams (Fig. 3). The spidergram is similar to the others from BM suite but its REE content is lower (Fig. 7).

The coincidence of the PT conditions of the black megacrysts and hydrous metasomatites supports the idea that the metasomatism was produced by intrusion of melts derived from fractionation of hydrous picrites at 3.5 GPa to hawaiites at 2, 5–2 GPa and mugearites near 1.5 GPa (see Fig. 5b). The decreasing liquidus line from alkali basalts (Rankenburg et al., 2004) to basanites (Esin et al., 1993) and mugearites (Irving and Green, 2008) crosses the PT path of the BMG. The water-bearing solidus for mugearites is near 700 °C at around 1 GPa (Irving and Green, 2008). Thus the entire range of pyroxenites from the BM suite may have been produced from such an evolving magma.

9.1.1. Fractionation

The increasing $(Gd/Yb)_n$ ratios and incompatible elements contents with decreasing temperatures during the magmatic fractionation suggests that garnet was precipitated together with clinopyroxene from the parental magma, allowing to calculate the Gar/Cpx ratio. Experimental data indicate the presence of garnet on the liquidus at 1350–1200 °C and 3.0–2.5 GPa in basanite and to 1.6 GPa under sub-liquidus conditions (Thompson, 1972; Arculus, 1975; Esin et al., 1993; Rankenburg et al., 2005) and to 1.2 GPa in hydrous melts (Mysen and Boettcher, 1975; Irving and Green, 2008). Ilmenite appears at about 1150–1000 °C (Thompson, 1972; Elthon, 1993), which agrees with the relative abundance of this phase in the final stages.

Despite the dependence of partition coefficients on temperatures (Wood and Blundy, 1997) and tschermakite content (Hill et al., 2000) taken into account in fractionation modeling in some studies (Dobosi and Jenner, 1999; Akinin et al., 2005), we have used constant Kd values (Hart and Dunn, 1993) because the experimental range of clinopyroxene Kd values for REE are not high within the 1400–1100 °C temperature interval (Hart and Dunn, 1993; Hauri et al., 1994; Schmidt et al.,1999; Johnson, 1998). Recombination of the Rayleigh fractionation equation:

$$C_i = C_0 f^{(D_{Bulk}-1)} \text{ to } f = e^{ln(C_i/C_0)/(D_{Cpx/melt}-1)}$$

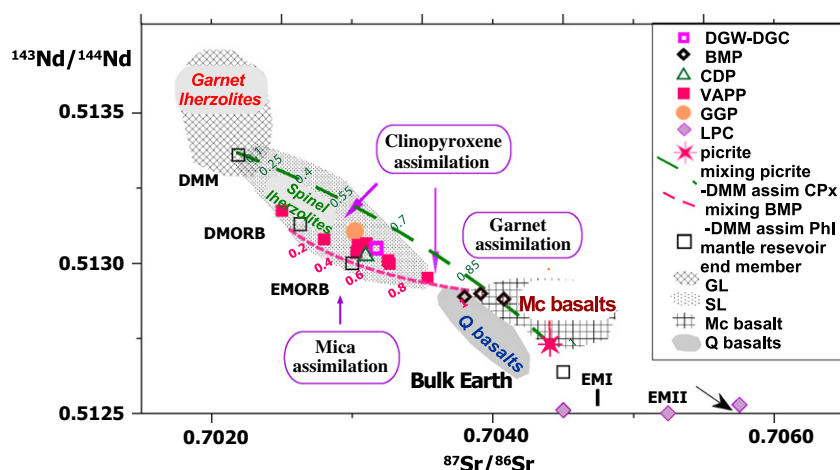gives the degree of magma fractionation between the nearest analyzed compositions of minerals with the trace element

Fig. 10. Compilation of $^{87}Sr/^{86}Sr$–$^{143}Nd/^{144}Nd$ isotope data for Vitim mantle xenoliths (Table 3). Data for lherzolites are from Ionov et al. (2005a) and Ionov et al., 2005 and for basalts after Johnson et al. (2005). The symbols for the pyroxenites are the same as for Fig. 3. (1) Garnet lherzolites; (2) Spinel lherzolites. (3) Post-erosion Plio-Pleistocene lavas from valley flows and scoria cones; (4) Miocene lava plateau flow; (5) Picrite basalts. Mixing lines are marked: AFC garnet lherzolite with mica and black pyroxenites parental melts (Miocene basalts); dashed AFC of melt parental for the black megapyropxenites and Cpx from garnet lherzolite.

concentrations C_i and C_0 respectively. They were determined for LREE where the input of the garnet partition coefficient in bulk partition coefficients $D_{i\ bulk}$ is negligible. Then for several MREE and HREE the bulk partition coefficient was found using the expression:

$$D_{bulk} = ln(C_i/C_0)/ln(f) + 1.$$

From the definition in each step, $D_{bulk} = \sum D_{imin/melt}X_i\ X_i$, where **X** is the fraction of mineral **i**. Solving these two equations for two MREE, it is possible to find the proportion of precipitated garnet and clinopyroxene in each stage. For better precision, several pairs of REE can be used. The degree of fractionation determined for the step from BMG to BMK is ∼40%. The trace element contents of the samples BMI (315-340) and BMK (315-133) were calculated from the same sample 315-174 which has a similar shaped spidergram. This suggests splitting of crystallization trends in the final stages, as seen in the variation diagrams (Fig. 3). The amount of garnet decreases from 15% to 17% in BMG and BM2 to 7–5% for BMI–BMK (Fig. 11A–C), which explains the rarity of garnets in pyroxenites which precipitated from more differentiated magmas.

The modeled trace element patterns differ from the spidergrams of the analyzed samples mainly by lower Hf and higher Zr concentrations, visible in the low temperature stages of crystallization. A possible reason is the variations of HFSE partition coefficients determined by the decreasing temperatures (Wood and Blundy, 1997; Blundy et al., 1998; Hill et al., 2000) during crystallization, Dobosi and Jenner (1999) used twice higher value of Kd for Zr then determined in the work of (Hart and Dunn, 1993). Lower Ba and Ti values of the modeled patterns suggest assimilation of some phases (probably phlogopite and ilmenite) by the parental magma (Fig. 12E and F).

9.1.2. Mixing

For the DGW-DGC series compared to the BMG pyroxenes lower overall trace element level, Gd/Yb$_n$ and Sm/La$_n$ ratios and enriched Cr content, La/Yb$_n$ and *mg*# correlated with the calculated temperatures suggest dissolution of solid material, probably by fractional crystallization with assimilation (AFC)(De Paolo, 1981; Neal and Davidson, 1989) (see Fig. 11D). Troughs at Zr and Ti in trace element diagrams cannot be a primary feature of parental basalts (Johnson et al., 2005) and suggest crystallization of minor phases including ilmenite. Assimilation of 7–10% of bulk solid peridotite with crystallization of clinopyroxene and 2–3% ilmenite, may account for the transition from primitive BMG composition to typical

DGW pyroxenes (see Fig. 12D). Elevated incompatible elements in sample 315-13 may result from admixture of low degree partial melts from GL in wall rocks.

The Sr–Nd isotopic data of BM pyroxenites plot on mixing lines between the picrite basalt compositions (Johnson et al., 2005) and DM sources. Those connecting the DMM and picrite-basalts assume dissolution of clinopyroxene having Sr/Nd < 1 and pass through the point for the typical BMG xenolith 315-254. The mixing line of this melt with phlogopite (Sr/Nd > 1) is traced by the VAPP compositions (Ionov et al., 2005a,b). The CDP and DGW pyroxenites plot between these two lines, indicating the presence of the hydrous phases in the melting source material for these pyroxenes. The Vitim Quaternary basalts continue the mixing lines of the CDP (or DGW) and picrite-basalt compositions, but the Miocene basalts show clear signatures of crustal contamination (Fig. 10).

9.1.3. Melting/selective phase dissolution of lherzolites and older metasomatic associations

Using the average bulk Vitim lherzolites (Ionov et al., 2005a,b) with a nearly flat chondrite-like REE pattern, with troughs in Zr, Th, Rb and slightly elevated Nb, Ta, Ba, Pb and Sr contents, as the melting material we modeled 1% partial melting and modal phase abundances for all parental melts for clinopyroxenes in green series as well as for the most primitive basaltic melts. Small minima in MREE typical of many green pyroxenites seem to be a result of selective clinopyroxene removal in previous stages.

Modeling of AFC (Rollinson, 1993) pyroxenite crystallization accompanied with melting of metasomatic associations using the partition coefficient for the common lherzolite silicate minerals (Bedard, 2006), ilmenites (Zack and Brumm, 1998), amphiboles (La Tourrette et al., 1995) and phlogopite (Foley et al., 1995, 1996) shows resulting LILE, HFSE enrichment of the precipitated clinopyroxenes (Fig. 11E). The contact zones of the large kaersutite veins contain clinopyroxenes that are enriched in HFSE with a peak in Ba, probably due to the phlogopite dissolution by melt. Melting of clinopyroxenes at the contacts and growth of hydrous minerals in the veins with their characteristic peaks can form the depressions of HFSE and concave-downward patterns of MREE found for phlogopites and GGP clinopyroxenes.

Finally, the slightly U-shaped REE distributions common for the Vitim bulk peridotites and ns (Ionov et al., 2005a,b; Glebovitskii et al., 2007) may appear after removal of clinopyroxene with humped REE distributions. Selective garnet dissolution during

Trace element patterns for pyroxenes
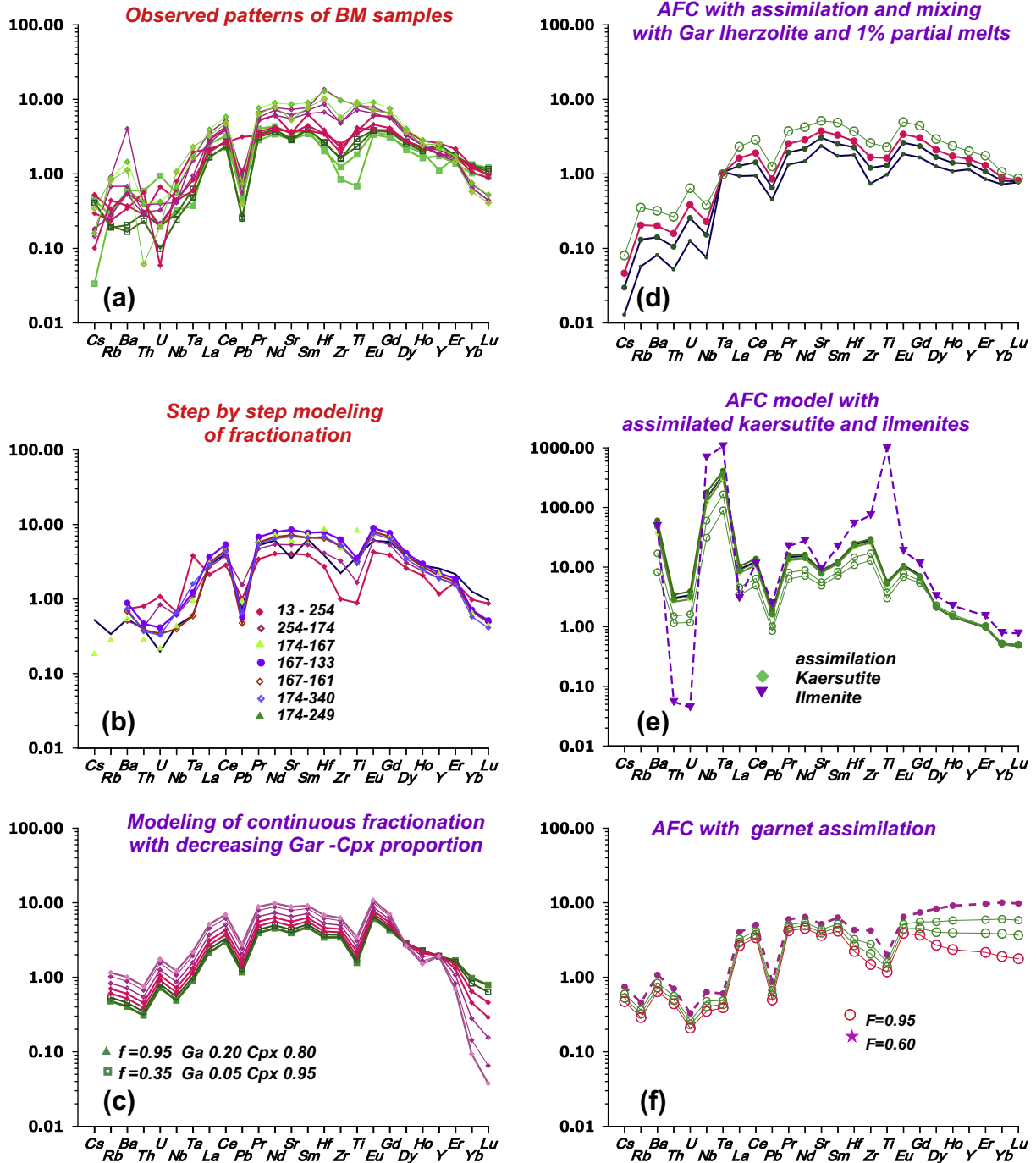## produced by fractionation and assimilation models

Fig. 11. Modeling of differentiation processes for pyroxenes from high temperature and black population of pyroxenes. (A) Observed patterns. (B) Modeling of the stepped differentiation from the starting pyroxene composition 315-254. For calculating the proportions of precipitated minerals, the partition coefficients for Cpx (Hart and Dunn, 1993) and garnet (Harte and Kirkley, 1997) were used; fractionation degrees and phase proportions for each step are as follows: (315) 13-254: f = 70%, 0.15 Ga, 0.85Cpx; (315) 254-174: f = 64%, 0.17 Ga, 0.83Cpx; (315) 174-167|: f = 57%, 0.07 Ga, 0.93Cpx; (315)167–161: f = 46%, 0.07 Ga, 0.93Cpx; (315)167–133: f = 44%, 0.065 Ga, 0.935Cpx; (315)174–340: f = 49%, 0.15 Ga, 0.85Cpx; (C) Modeling of the fractionation with reduction of garnet proportion from 20% to 5%. (D) Modeling of mixing basaltic magma with average Vitim peridotite (Ionov et al., 2005a) (+1% partial melt); (E) AFC with the assimilation of 5 wt.% of kaersutite, ilmenite which increase HFSE content; (F) AFC assimilation of garnet and clinopyroxene crystallization. Partition coefficients for peridotites from compilation of Bedard (2006), for amphibole (Brenan et al., 1996; Dalpé and Baker, 2000), for phlogopite (Foley, 1992), ilmenites after Zack and Brumm (1998).

AFC process (De Paolo, 1981; Neal and Davidson, 1989) may decrease HREE content (see supplemental file 5). Peaks and troughs in the LILE and HFSE may be result of the melting of metasomatites containing micas and amphiboles (Kalfoun et al., 2002; Fulmer et al., 2010).

9.2. Relation with erupted basaltic magmas

Megacrysts have often been suggested to be precipitates from their host basalts (Frey, 1980; Aoki and Fujimaki, 1984; Dobosi and Jenner, 1999), but in most cases they differ in isotopic features

**Parent melts for Cpx
for different types of pyroxenites**
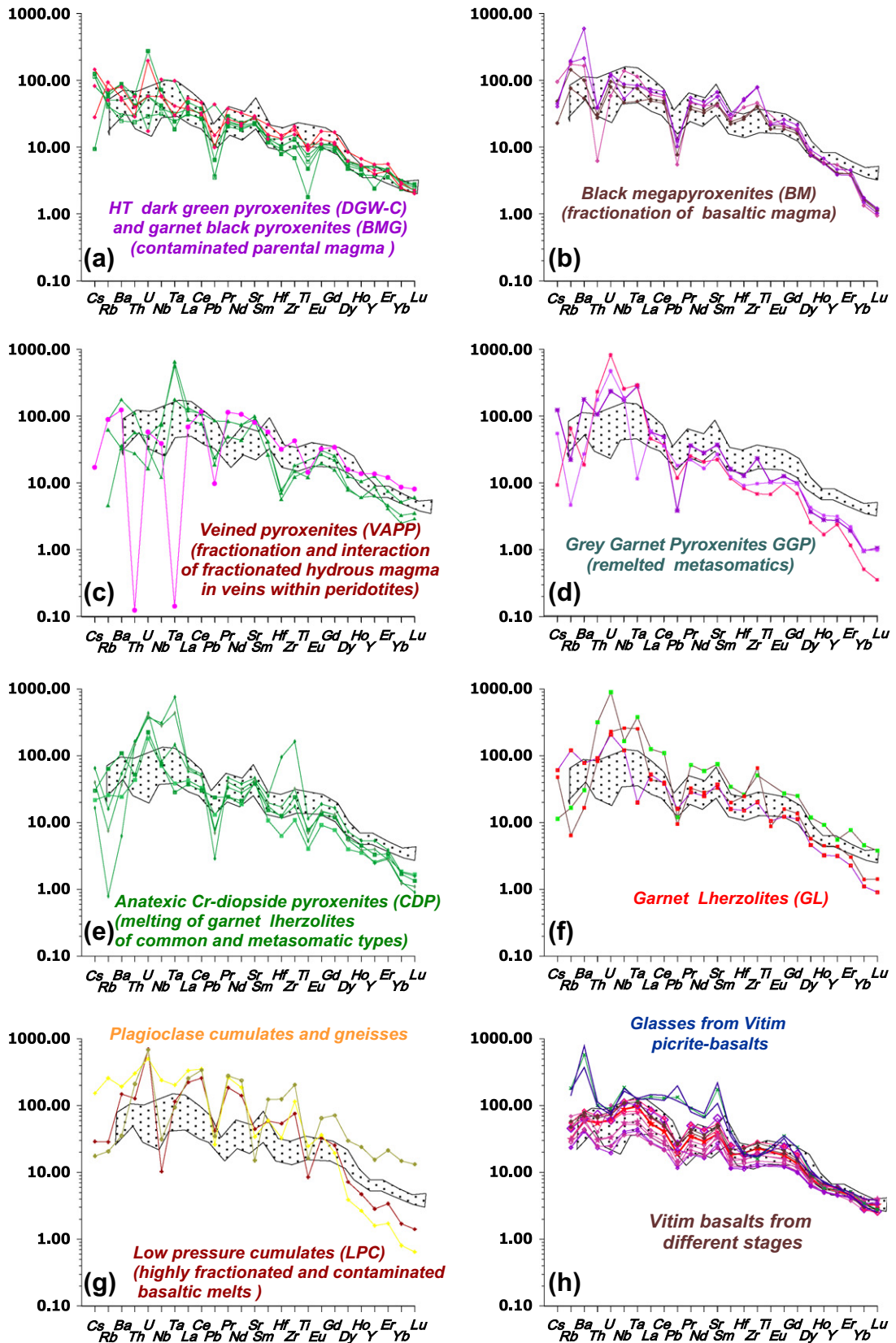
Fig. 12. Primitive mantle-normalized spidergrams of parental melts for different groups of Vitim xenoliths, in comparison with those for erupted basalts (Johnson et al., 2005). Partition coefficients for the calculation of clinopyroxene parental magma from Hart and Dunn (1993).

and trace elements (Aspen et al., 1990; Liu et al., 1992; Hegner et al., 1995; Barron et al., 1996; Lee et al., 1996; Witt-Eickschen and Kramm, 1998; Rankenburg et al., 2005). Calculated parental melts for the BMG group, slightly differ from Vitim picrite-basalts, in having lower Pb content and $(La/Yb)_n$ ratios (Fig. 12). The other BM groups have higher $(La/Yb)_n$ and show a stronger Fe# increase.

Partial melting (1%) of average Vitim lherzolite (Ionov et al., 2005a,b; Glebovitskii et al., 2007) can produce a trace element pattern nearly coincident with that of Pleistocene basanites from Kandidushka volcano and other Vitim plateau alkali basalts (Johnson et al., 2005), except for LIL elements (see supplemental file 5). Modeling of the composition of the primitive alkali olivine basalts and basanites from the lower part of plateau requires 1.5–2% melting. Calculated parental melts for DGW and some BMG (0.1–0.75 wt.% Cr_2O_3) (after multiplying by the Kd of Hart and Dunn, 1993) clinopyroxenes are close in Mg# and Cr values (400–40 ppm) (Esin et al., 1995; Johnson et al., 2005) to the values typical for basalts. The more evolved BM2 – BMI groups are far from equilibrium with the basalts. PT conditions determined for basaltic liquids according to Albarede (1992) thermobarometry give quite good agreement with the high temperature branch of BMG (Ashchepkov et al., 2003).

Hypotheses of the metasomatic origin of the BM suite similar to those suggested for kimberlitic megacrysts (Pivin et al., 2009; Kopylova et al., 2009) cannot be applied due to the good correlations between Fe# and TiO_2 while metasomatites may show negative tendencies. Euhedral cut crystals may be formed probably may be formed in cavities in magma channels forming during pressure decrease and degassing.

9.3. How many melts were there?

The coexisting melts for pyroxenites reconstructed with $D_{Cpx/melt}$ (Hart and Dunn, 1993) show wide variations (Ashchepkov et al., 1995b) (Fig. 12) suggesting that several different melts were involved in pyroxenite formation. Similarities in REE of parental melts for BMG, DGW, CDP and lherzolites with the OIB-type basalts are explained by 1% melting of primitive garnet lherzolites which is considered to be the critical melt fraction in the intergranular space (McDonough and Sun, 1995). Melting of mantle eclogites and pyroxenites is thought to be the source of OIB basalts (Cordery et al., 1997; Kogiso et al., 1998; Sobolev et al., 2005) while Vitim basalts and BM pyroxenes have smooth spidergrams (Johnson et al., 2005) and most fluctuations are formed by admixture of metasomatites and fluid which produce Ba, Pb, Sr, HFSE peaks, or intergranular material (Bodinier et al., 1996).

The following types of melt are considered to have been formed separately:

(1) picrite-basalts and fractionated derivates, of which there are two main varieties: (a) high temperature (>1200 °C) primitive or contaminated melts which produced the DGW-DGC and BMG series; (b) evolved melts parental to the BMP which crystallized the clinopyroxene megacrystalline suite and the Al-augite veins cutting peridotites (final differentiates from the picrite-basaltic liquid); (2) partial melts that produced clinopyroxene in lherzolites and Cr-diopside pyroxenites (28–48 Ma) according to Sm–Nd isotopic analyses of Gar–Cpx pairs (Ionov et al., 1995) and an Ar/Ar isochron (laser $^{40}Ar/^{39}Ar$ dating of mica for mica), while Lu–Hf analyses of mineral pairs yielded an age of 30–75 Ma (Ionov, 2007; (3) hybrid melts which produced the GGP, contaminated by earlier metasomatic assemblages; (4) Fe-rich melts responsible for shallow cumulates probably produced by the remaining basaltic melts interacting with crustal rocks.

Comparison of the glasses and pyroxenes from picrite basalts (Fig. 12H, Table 1, supplemental file 1), the compositions of erupted lavas (Johnson et al., 2005) and parental melts for the DGW, DGW, BMG types shows clear similarities in their Sr–Ba peaks and Zr troughs. Parental melts for BM with Pb minima typical of fractionation processes, and LILE and HFSE fluctuations due to mixing with melted of intergranular material from wall rocks have no exact analogies in Vitim plateau lavas (Johnson et al., 2005). The parental melts for the GGP group had high volatile content elevated incompatible element contents, with a peak at Nb, minimum in Zr and inflected REE patterns due to melting of hydrous metasomatites by the hot alkaline basalt magmas. The anatectic melts which formed CDP had higher LILE and U-Th contents and enrichment in Zr and Hf than typical Vitim alkali basalts which show only moderate enrichment in incompatible elements.

9.4. Megacrysts – the path of rising melts?

BM pyroxenites form a nearly continuous series in which the abundance of the samples in group relative to amount of the whole population is inversely correlated in general with the degree of fractionation. The parental melts for BM pyroxenites must have evolved rapidly in a system separated from the main volume of basaltic magma. The highest temperature Cr-rich varieties were buffered in mg# by the surrounding peridotites until 1200–1250 °C, but then they quickly differentiated during cooling. The BM suite forms a polybaric sequence that evolved from garnet- to plagioclase-bearing assemblages. The complex structure and P–T estimates, and rare direct contacts with peridotites prove their origin in mobile magmatic systems developed in the peridotitic lithosphere. In the giant-grained pyroxenites, the abundance of volatiles in the parental melt is evidenced by the abundance of gaseous cavities. The most differentiated melts became extremely enriched in fluid including H_2O and crystallized Ti-biotites their position near the Moho boundary may suggest some influence of volatiles from the crust and increase of oxidation state.

These conditions may have existed in a system of connected networks of large veins, dykes and magma chambers. They may have formed during boiling at the top of basaltic reservoirs and risen up in fractures formed by hydraulic fracturing (Sobolev and Siplivets, 1987). When the fracture stops opening, rising magma creates a magma chamber or network of pegmatite-like large veins. This is supported by the isobaric PT ranges for the several groups (BMG, BM1, and BM2) in the PT diagrams. Plating of crystals on the walls of developing veins (Wilshire et al., 1980) would result in rapid fractionation of the melts. Accumulation of volatiles was followed by new steps of upward intrusion. The steps accompanied by the branching of fractures may be recognized by jumps in the Cr content in the pyroxenites, probably created in the apophyses in conducting veins or during the assimilation of contaminated peridotites in the initial pulse. Judging from the detailed reconstruction of mantle temperature sections beneath the Vitim area (Ashchepkov et al., 1994; 2003), the dense network of the VAPP, CDP and GGP veins was probably located close to BM bodies formed of basaltic precipitates (Fig. 13). Their origin may have been initiated by heating and volatile fluxes from basaltic magmas. Discontinuities of mantle structure and phase boundaries such as Gar–Sp transitions may have stopped the development of fractures and given rise to dense vein systems.

When the system stopped rising rapidly due to low magma volume or escape of volatiles, replenishment from beneath provided more magma for further movement. This may have been accompanied by dissolution of already partly solidified material and saturation in incompatible components due to selective melting of metasomatites including ilmenites, micas and kaersutites formed in the previous stages mainly in contact zones and intergranular space. The BM suite reveals direct evidence of replenishment, seen
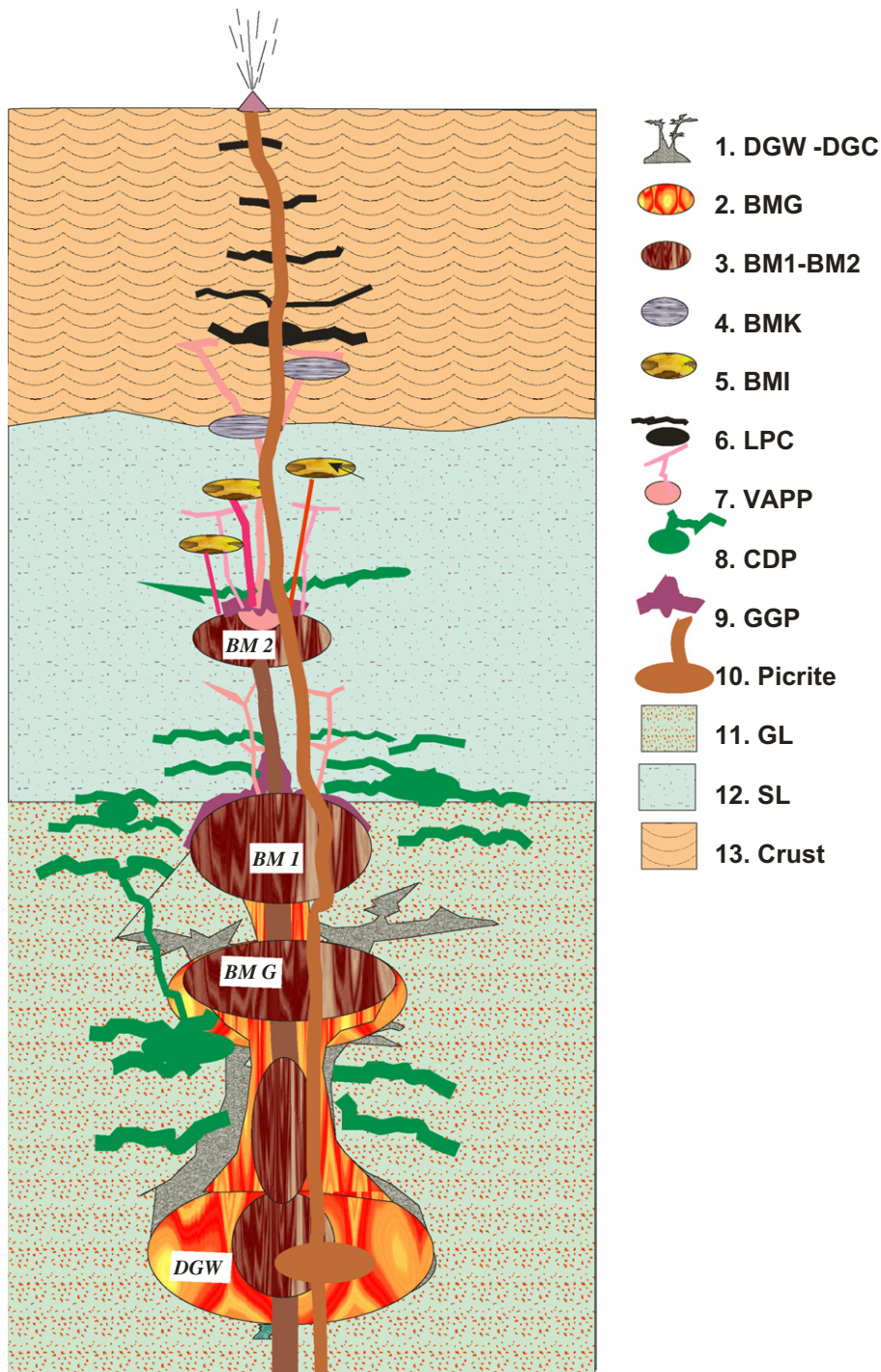
Fig. 13. Schematic development of the vein system in the mantle beneath Vitim for the picrite basalt stage of magmatism.

in the deformation of BM megacrystalline pyroxenite series and several trajectories on PT diagrams (Fig. 4).

Comparing the PT conditions for the megacrysts, it is clear that clusters and breaks of the PT paths coincide with phase boundary transitions. The deepest varieties started from the ~3.0 GPa minimum in the water-bearing solidus. They crystallized pyrope almandine garnets (Arculus, 1975; Ashchepkov et al., 1996). The water-bearing magmas were co-precipitated garnet, clinopyroxene, mica and kaersutite (Mysen and Boettcher, 1975; Irving and Green, 2008; Knutson and Green, 1975) in Bartoy (Ionov et al., 1992; Ashchepkov et al., 2003) and Minusa (Ashchepkov et al.,

1995a) usually are forming magmatic chambers near 2.0 GPa (Fig. 6b).

The pressure histograms for lherzolites and pyroxenites including CDP and BM series are rather similar (supplemental file 4). All types of xenoliths are likely to have been captured mainly near the discontinuities of the feeding melt system where the magma may have changed its ascent rate (Sobolev and Siplivets, 1987) often in the roof of magmatic chambers. Judging by complex contacts, ascending basaltic magmas may have used the same channels repeatedly, forming dyke-in-dyke structures as in ophiolites (Dobretsov and Ashchepkov, 1991).

After the step by step ascent of the most differentiated melt portions from the basaltic intrusion to the boundary of the spinel facies, the melts reached the temperature conditions of the lherzolites at ∼2.0 GPa close to the dry solidus. The last differentiated magma portions were supersaturated in volatiles and easily intruded the crust. Self-oxidation of the remaining melt portions caused ilmenites and then Ti-magnetites and alkali feldspars from the remaining melt. Melting of gneisses in crust resulted in the further enrichment in volatiles and Ti-biotite and amphibole crystallization.

A schematic model for the development of the pre-eruption basaltic veins in the mantle beneath Vitim is shown in Fig. 13. Multistage stepped ascent of magma in the fractures, accompanied by differentiation and dissolution of wall rocks, formed the compositional variation seen in the BM suite.

10. Conclusions

(1) Megacrystalline clinopyroxenite xenoliths carried by Vitim picrite basalts were formed in a polybaric vein system with four main levels of magma fractionation: near 3.3–2.3, 2.2–2.0, 1.9–1.5 and 1.3–1.0 GPa, in a temperature range of 1350–900 °C.

(2) Formation of the differentiated coarse- to giant-grained pyroxenite xenoliths was related to development of a pre-eruption vein system within the lithospheric mantle.

(3) The major and trace element variations can be accounted for by cotectic crystallization of garnet and clinopyroxene with the modal fraction of garnet decreasing from 17–15% to 5–7%, and, during the final stages, by crystallization of clinopyroxene plus ilmenite (+Ti-biotite) in relatively closed vein systems. Exchange with the wall-rock peridotites occurred only at relatively high-T (>1300 °C) and ceased below 1200 °C.

(4) Stepped melt intrusions was accompanied by fracturing and partial dissolution of previously formed augite pyroxenites and surrounding metasomatites.

(5) The main levels of megacryst capture coincided with those of lherzolites and pyroxenite xenoliths in the mantle beneath the Vitim area.

Acknowledgements

Appendix A

For the pyroxenite and high Al–Cr-diopside compositions (see correlations on Fig. 4b) the barometer (Ashchepkov et al., 2010) was rearranged to by the adding the temperature influence on Al, Ta, Fe exactly in KD as following:

$$P(Ash2011) = 0.3 * XAlCr * T°K/(1 + 2.35 * Fe + Fe * (T°C$$
$$- 600)/800) - 40 * \ln(1273/T°C) * (7 * Na + 10$$
$$* Cr15 + Mg/4 - Al - 15 * Ti) + 50 * (Na + 0.2 * Al$$
$$- 2 * Ti + 0.05 * Mg - 0.22 * Ca - 0.7 * Na/Ca)$$
$$+ 7.5 * Si - 20 * Al * Na * Mg/Ca/(Al + Na - 2 * Ti$$
$$- 2 * Fe3+)$$

where $KD = Na * Mg/XAlCr*/Ca$;

$$XAlCr = (Al - 0.01) * ((T°K - 600)/700)^{3/4} + Cr * ((T°K$$
$$- 100)/900 - K + (4 * Ti - 0.0125)/(T°K - 800) * 700$$
$$+ (Fe - 0.23) * (T°K - 900)/10000$$

This equation give good PT conditions for lherzolites, Al – augites and omphacites.

The program (DOS) for the PT estimates (ter55LA.rar) and files of the data for calculations are available as supplemental files and on site http://igc.igm.nsc.ru/ash/index.htm and new version by e-mail: Igora57@mail.ru; Igor.Ashchepkov@igm.nsc.ru.

Appendix B. Supplementary data

Supplementary data associated with this article can be found, in the online version, at doi:10.1016/j.jseaes.2011.03.004.

References

Adam, J., Green, T., 2006. Trace element partitioning between mica- and amphibole-bearing garnet lherzolite and hydrous basanitic melt: 1. Experimental results and the investigation of controls on partitioning behaviour. Contributions to Mineralogy and Petrology 152, 1–17.

Akinin, V.V., Roden, M.F., Francis, D., Apt, J., Moll-Stalcup, E., 1997. Compositional and thermal state of the upper mantle beneath the Bering Sea basalt province: evidence from the Chukchi Peninsula of Russia. Canadian Journal of Earth Sciences 34, 789–800.

Akinin, V.V., Sobolev, A.V., Ntaflos, T., Richer, W., 2005. Clinopyroxene megacrysts from Enmelen melanephelinitic volcanoes (Chukchi Peninsula, Russia): application to composition and evolution of mantle melts. Contributions to Mineralogy and Petrology 150, 85–1101.

Albarede, F., 1992. How deep do common basaltic magmas form and differentiate. Journal of Geophysical Research 97, 10997–11009.

Anderson, T., Griffin, W.L., O'Reilly, S.Y., 1987. Primary sulfide melt inclusions in mantle derived megacrysts and pyroxenites. Lithos 20, 279–294.

Andre, L., Ashchepkov, I.V., 1996. Acid leaching experiments on the mantle derived Vitim pyroxenites: implications for the role of clinopyroxenes in the mantle processes. In: Demaiffe, D. (Ed.), Petrology and Geochemistry of Magmatic Sites of Rocks in the Continental and Oceanic Crust. Universite Libre de Bruxells. Royal Museum for Central Africa (Tervuren), pp. 321–336.

Aoki, K., Fujimaki, H., 1984. REE abundances in exsolved garnet-bearing clinopyroxene megacryst from Bellsbank kimberlite (South Africa). Chemical Geology 45, 165–171.

Arculus, R.J., 1975. Melting behavior of two basanites in range 10 to 35 GPa and effect of TiO_2 on the olivine – diopside reactions at high pressures. Carnegie Institute Washington Yearbook 74, 512–515.

Ashchepkov, I.V., Dobretsov, N.L., Kalmanovich, M.A., 1989. Garnet peridotite xenoliths from alkalic picritoid and basanitoid of the Vitim Plateau. Transactions of USSR Academy of Sciences, Earth Science Section 302, 156–159.

Ashchepkov, I.V., 1991. Mantle Xenoliths of the Baikal Rift. Nauka, Novosibirsk, 160 p (in Russian).

Ashchepkov, I.V., Litasov, Y.D., Dobretsov, N.L., 1994. Pyroxenites and complex garnet peridotites from picrite-basalts, Vitim plateau (Trans Baikal): implication for thermobarometry and mantle reconstruction. In: Kimberlites, Related Rocks and Mantle Xenoliths, Special Issue 1/A, Companhia de Pesquisa de Recursos Minerais (CPRM), Rio de Janeiro, Brasil, pp. 455–467.

Ashchepkov, I.V., Kepezhinskas, V.V., Malkovets, V.G., Ovchinnikov, Y.I., 1995a. Mantle Xenoliths from the Meso-Cenozoic Volcanic Pipes of Khakassia: Field Guide Book: 6th Int. Kimberlite Conf, Novosibirsk. 39 p.

Ashchepkov, I.V., Andre L., Litasov, K.D., Malkovets, V.G., 1995b. Origin and evolution of mantle melts Beneath Vitim plateau. Extended abstracts 6th Int. kimberlite conf. Novosibirsk, Novosibirsk, pp. 17–19.

Ashchepkov, I.V., Litasov, Yu.D., Litasov, K.D., 1996. Xenoliths of garnet xenoliths from nephelinites, the Khentey ridge (Southern Transbaikalia): evidence of the mantle diapir ascend. Russian Geology and Geophysics 37, 121–137.

Ashchepkov, I.V., Andre, L., 2002. Differentiation of the mantle melts: an example of the pyroxenite xenoliths from picrite basalts Vitim plateau. Russian Geology and Geophysics 43 (4), 343–363.

Ashchepkov, I.V., 2002. An empirical clinopyroxene thermobarometer for mantle rocks based on the jadeite-diopside exchange. Transactions of Russian Academy of Sciences, Earth Section 382, 78–82.

Ashchepkov, I.V., Travin, S.V., Saprykin, A.I., Andre, L., Gerasimov, P.A., Khmel'nikova, O.S., 2003. Age of xenolith-bearing basalts and mantle evolution in the Baikal rift zone. Russian Geology and Geophysics 44, 1160–1188.

Ashchepkov, I.V., Pokhilenko, N.P., Vladykin, N.V., Logvinova, A.M., Kostrovitsky, S.I., Afanasiev, V.P., Pokhilenko, L.N., Kuligin, S.S., Malygina, L.V., Alymova, N.V., Khmelnikova, O.S., Palessky, S.V., Nikolaeva, I.V., Karpenko, M.A., Stagnitsky, Y.B., 2010. Structure and evolution of the lithospheric mantle beneath Siberian craton, thermobarometric study. Tectonophysics 485, 17–41.

Aspen, P., Upton, B.G.J., Dickin, A.P., 1990. Anorthoclase, sanidine and associated megacrysts in Scottish alkali basalts; high-pressure syenite debris from upper mantle sources. European Journal of Mineralogy 2, 503–517.

Barron, B.J., Robertson, A.D., Sutherland, F.L., 1996. Olivine 'leucitites', their xenolith and megacryst suites, Hoskings peaks, north Queensland. Australian Journal of Earth Sciences 43, 231–244.

Bedard, J.H., 2006. A catalytic delamination-driven model for coupled genesis of Archaean crust and sub-continental lithospheric mantle. Geochimica et Cosmochimica Acta 70, 1188–1214.

Beeson, M.H., Jackson, E.D., 1970. Origin of the garnet pyroxenite xenoliths from Salt Lake Crater Oahu, vol. 3. Spec. Pap. Min. Soc. Am., pp. 95–112.

Bjerg, E.A., Ntaflos, T., Kurat, G., Dobosi, G., Labudía, C.H., 2005. The upper mantle beneath Patagonia, Argentina, documented by xenoliths from alkali basalts. Journal of South American Earth Sciences 18, 125–145.

Blundy, J.D., Robinson, J.A.C., Wood, B.J., 1998. Heavy REE compatible in clinopyroxene on the spinel lherzolite solidus. Earth and Planetary Science Letters 160, 493–504.

Bodinier, J.-L., Merlet, C., Bedini, R.M., Simien, F., Remaidi, M., Garrido, C.J., 1996. Distribution of niobium, tantalum, and other highly incompatible trace elements in the lithospheric mantle: the spinel paradox. Geochimica et Cosmochimica Acta 60, 545–550.

Brenan, J.M., Shaw, H.F., Ryerson, F.J., Phinney, D.L., 1996. Experimental determination of trace-element partitioning between pargasite and a synthetic hydrous andesitic melt. Earth and Planetary Science Letters 140, 287–288.

Brey, G.P., Kohler, T., 1990. Geothermobarometry in four phase lherzolites II: new thermobarometers and practical assessment of using thermobarometers. Journal of Petrology 31, 1353–1378.

Brassinnes, S., Balaganskaya, E., Demaiffea, D., 2005. Magmatic evolution of the differentiated ultramafic, alkaline and carbonatite intrusion of Vuoriyarvi (Kola Peninsula, Russia). A LA-ICP-MS study of apatite. Lithos 85, 76–92.

Brey, G.P., Bulatov, V.K., Girnis, A.V., 2008. Geobarometry for peridotites: experiments in simple and natural systems from 6 to10 GPa. Journal of Petrology 49, 3–24.

Chapman, N.A., 1976. Inclusions and megacrysts from undersaturated tuffs and basanites, East Fife, Scotland. Journal of Petrology 17, 472–498.

Chazot, G., Menzies, M.A., Harte, B., 1995. Determination of partition coefficients between apatite, clinopyroxene, amphibole, and melt in natural spinel lherzolites from Yemen: implications for wet melting of the lithospheric mantle. Geochimica et Cosmochimica Acta 60, 423–437.

Choi, S.H., Mukasa, S.B., Zhou, X.-H., Xian, X.H., Andronikov, A.V., 2008. Mantle dynamics beneath East Asia constrained by Sr, Nd, Pb and Hf isotopic systematics of ultramafic xenoliths and their host basalts from Hannuoba, North China. Chemical Geology 248 (2008), 40–61.

Cordery, M.J., Davies, G.F., Campbell, I.H., 1997. Genesis of flood basalts from eclogite bearing mantle plumes. Journal of Geophysical Research 102B9, 20179–20197.

Dalpé, C., Baker, D.R., 2000. Experimental investigation of large-ion-lithophile element, high-field-strength-element and rare-earth-element partitioning between calcic amphibole and basaltic melt: the effects of pressure and oxygen fugacity. Contributions to Mineralogy and Petrology 140, 233–250.

Dasgupta, R., Hirschmann, M.M., Smith, N.D., 2007. Partial melting experiments of peridotite CO₂ at 3 GPa and genesis of alkalic ocean island basalts. Journal of Petrology 44, 2173–2201.

Delaney, J.S., Smith, J.V., Nixon, P.H., 1979. Model for upper mantle below Malaita, Solomon Islands, deduced from chemistry of lherzolite and megacryst minerals. Contributions to Mineralogy and Petrology 70, 209–218.

De Paolo, D.J., 1981. Trace element and isotopic effects of combined wall rock assimilation and fractional crystallization. Earth and Planetary Science Letters 53, 189–202.

Dobosi, G., Jenner, G.A., 1999. Petrologic implications of trace element variation in clinopyroxene megacrysts from the Nógrád volcanic province, north Hungary: a study by laser ablation microprobe-inductively coupled plasma-mass spectrometry. Lithos 46, 731–749.

Downes, H., 1993. The nature of the lower continental crust of Europe: petrologic and geochemical evidence from xenoliths. Physics of the Earth and Planetary Interiors 79, 195–218.

Downes, H., 2001. Formation and modification of the shallow sub-continental lithospheric mantle: a review of geochemical evidence from ultramafic xenolith massifs of Western and Central Europe. Journal of Petrology 42, 233–250.

Downes, H., 2007. Origin and significance of spinel and garnet pyroxenites in the shallow lithospheric mantle: ultramafic massifs in orogenic belts in Western Europe and NW Africa. Lithos 99, 1–24.

Dobretsov, N.L., Ashchepkov, I.V., 1991. Melt migration and depletion-regeneration processes in upper mantle of continental and ocean rift zones. In: Ophiolite Genesis and Evolution of the Oceanic Lithosphere: Proceedings of the Ophiolite Conference, held in Muscat, Oman, 7–18 January 1990, Kluwer Academic Publishers, pp. 125–146.

Dobretsov, N.L., Ashchepkov, I.V., Simonov, V.A., Zhmodic, S.M., 1992. Interaction of the mantle rocks with the fluids and melts in Baikal rift zone. Russian Geology and Geophysics 34 (5), 3–21.

Edgar, A.D., 1987. The genesis of alkaline magmas with emphasis on their source region: inferences from experimental studies. In: Fitton, J.G., Upton, B.G.J. (Eds.), Alkaline Igneous Rocks, vol. 30. Geological Society London Special Publication, pp. 29–52.

Eggler, D.H., Mccallum, M.E., 1976. A geotherm from megacrysts in the Sloan kimberlite pipes, Colorado, vol. 75. Carnegie Inst. Wash. Yearb.. pp. 538–541.

Elthon, D., 1993. The crystallization of mid-ocean ridge basalts at moderate and high pressures. European Journal of Mineralogy 5 (6), 1025–1037.

Esin, S.V., Logvinov, V.M., Ashchepkov, I.V., 1993. Megacrysts of alumina clinopyroxenes from the Minusa depression, Baikal Rift Zone and Eastern Sikhote-Alin. Russian Geology and Geophysics 34, 81–89.

Esin, S.V., Ashchepkov, I.V., Ponomarchuk, V.A., et al., 1995. Petrogenesis of alkaline basaltoids from the Vitim plateau Baikal Rift Zone. UIGGM, Siberian Branch. Russian Academy of Sciences Press, Novosibirsk. pp. 1–58.

Foley, S.F., 1992. Vein- plus- wall-rock melting mechanism in the lithosphere and the origin of potassic alkaline magma. Lithos 28, 435–453.

Foley, S.F., Jenner, G.A., Konzet, J., Sweeney, R.J., 1995. Trace element partitioning in natural phlogopite and K-richterite-bearing xenoliths from Southern Africa kimberlites. In: Sixth International Kimberlite Conference, Extended Abstracts, UIGGM SD RASc, Novosibirsk, Russia, pp. 164–166.

Foley, S.F., Jackson, S.E., Fryer, B.J., Greenough, J.D., Jenner, G.A., 1996. Trace element partition coefficients for clinopyroxene and phlogopite in an alkaline lamprophyre from Newfoundland by LAM-ICP-MS. Geochimica et Cosmochimica Acta 60, 629–638.

Foley, S.F., Yaxley, G.M., Rosenthal, A., Buhre, S., Kiseeva, E.S., Rapp, R.P., Jacob, D.E., 2009. The composition of near-solidus melts of peridotite in the presence of CO₂ and H₂O between 40 and 60 kbar. Lithos 112 (S1), 274–283.

Frey, F.A., Printz, M., 1978. Ultramafic inclusions from San Carlos, AZ: petrologic and geochemical data bearing on their petrogenesis. Earth and Planetary Science Letters 38, 129–176.

Frey, F.A., 1980. The origin of pyroxenites and garnet pyroxenites from Salt Lake Crater, Oahu, Hawaii: trace element evidence. American Journal of Science 280, 427–449.

Fulmer, E.C., Nebel, O., van Westrenen, W., 2010. High-precision high field strength element partitioning between garnet, amphibole and alkaline melt from Kakanui. New Zealand Original Research Article Geochimica et Cosmochimica Acta 74, 2741–2759.

Glaser, S.M., Foley, S.F., Gunther, D., 1999. Trace element compositions of minerals in garnet and spinel peridotite xenoliths from the Vitim volcanic field, Transbaikalia, eastern Siberia. Lithos 48, 263–285.

Glebovitskii, V.A., Nikitina, L.P., Saltykova, A.K., Pushkarev, Yu.D., Ovchinnikov, M.S., Babushkina, N.O., Ashchepkov, I.V., 2007. Thermal and Chemical Heterogeneity of the Upper Mantle beneath the Baikal–Mongolia Territory. Petrology 15, 58–89.

Govindaraju, K., 1988a. Compilation of working values and sample description for 272 geostandards. Geostandards Newsletter 13 (spec. iss.).

Govindaraju, K., 1988b. Compilation report on trace elements in six ANRT rock reference samples: Diorite DR-N, Serpentinite UB-N, Bauxite BX-N, Disthene DT-N, Granite GS-N and Potash feldspar FK-N. Geostandards Newsletter 13, 5–67.

Griffin, W.L., O'Reilly, S.Y., Stabel, C.G., 1988. Mantle metasomatism beneath western Victoria, Australia: II. Isotopic geochemistry of Cr-diopside lherzolites and Al-augite pyroxenites. Geochimica et Cosmochimica Acta 52, 449–459.

Hart, S.R., Dunn, T., 1993. Experimental cpx/melt partitioning of 24 trace elements. Contributions to Mineralogy and Petrology 113, 1–8.

Harte, B., Kirkley, M.B., 1997. Partitioning of trace elements between clinopyroxene and garnet: data from mantle eclogites. Chemical Geology 136, 1–24.

Hauri, E.H., Wagner, T.P., Grove, T.L., 1994. Experimental and natural partitioning of Th, U, Pb and other trace elements between garnet, clinopyroxene and basaltic melts. Chemical Geology 117, 149–166.

Hegner, E., Walter, H.J., Satir, M., 1995. Pb-Sr-Nd isotopic compositions and trace element geochemistry of megacrysts and melilitites from the Tertiary Urach volcanic field: Source composition of small volume melts under SW Germany. Contributions to Mineralogy and Petrology 122 (3), 322–335.

Hill, E., Wood, B.J., Blundy, J.D., 2000. The effect of Ca-Tschermaks component on trace element partitioning between clinopyroxene and silicate melt. Lithos 53, 203–215.

Huang, X.-L., Xu, Y.-G., Lo, C.-H., Wang, R.-C., Lin, C.-Y., 2007. Exsolution lamellae in a clinopyroxene megacryst aggregate from Cenozoic basalt, Leizhou Peninsula, South China: petrography and chemical evolution. Contributions to Mineralogy and Petrology 154, 691–705.

Ionov, D.A., Kramm, U., Stosch, H.-G., 1992. Evolution of the upper mantle beneath the southern Baikal rift zone: an Sr-Nd study of xenoliths from the Bartoy volcanoes. Contributions to Mineralogy and Petrology 111, 235–247.

Ionov, D.A., Ashchepkov, I.V., Stosch, H.-G., Witt-Eickschen, G., Seck, H.A., 1993. Garnet peridotite xenoliths from the Vitim Volcanic Field, Baikal Region – the nature of the garnet spinel peridotite transition zone in the continental mantle. Journal of Petrology 34, 1141–1175.

Ionov, D.A., O'Reilly, S.Y., Ashchepkov, I.V., 1995. Feldspar-bearing iherzolite xenoliths in alkali basalts from Hamar–Daban, southern Baikal region, Russia. Contributions to Mineralogy and Petrology 122, 174–190.

Ionov, D.A., Hofmann, A.W., 1995. Nb–Ta- rich mantle amphiboles and micas: implication for subduction related trace element fractionation. Earth and Planetary Science Letters 131, 341–356.

Ionov, D.A., Ashchepkov, I., Jagoutz, E., 2005a. The provenance of fertile off-craton lithospheric mantle: Sr–Nd isotope and chemical composition of garnet and spinel peridotite xenoliths from Vitim, Siberia. Chemical Geology 217, 41–75.

Ionov, D.A., Blichert-Toft, J., Weis, D., 2005b. Hf isotope compositions and HREE variations in off-craton garnet and spinel peridotite xenoliths from central Asia. Geochimica et Cosmochimica Acta 69, 2399–2418.

Ionov, D.A., 2007. Compositional variations and heterogeneity in fertile lithospheric mantle: peridotite xenoliths in basalts from Tariat, Mongolia. Contributions to Mineralogy and Petrology 154, 455–477.

Ionov, D.A., Hofmann, A.W., 2007. Depth of formation of subcontinental off-craton peridotites. Earth and Planetary Science Letters 261, 620–634.

Irving, A.J., 1980. Petrology and geochemistry of composite ultramafic xenoliths in alkalic basalts and implications for magmatic processes within the mantle. American Journal of Science 280A, 389–426.

Irving, A.J., 1984. Polybaric mixing, fractionation of alkalic magmas; evidence from megacryst suites. AGU 1984 fall meeting. Eos, Transactions American Geophysical Union 65, 1153.

Irving, A.J., Frey, F.A., 1984. Trace element abundances in megacrysts and their host basalts: constraints on partition coefficients and megacryst genesis. Geochimica et Cosmochimica Acta 48, 1201–1221.

Irving, A.J., Green, D.H., 2008. Phase relationships of hydrous alkalic magmas at high pressures: production of nepheline hawaiitic to mugearitic liquids by amphibole-dominated fractional crystallization within the lithospheric mantle. Journal of Petrology 49, 741–756.

Johnson, K.T.M., 1998. Experimental determination of partition coefficients for rare earth and high-field-strength elements between clinopyroxene, garnet, and basaltic melt at high pressures. Contributions to Mineralogy and Petrology 133, 60–68.

Johnson, J.S., Gibson, S.A., Thompson, R.N., Nowell, G.M., 2005. Volcanism in the Vitim Volcanic Field, Siberia: geochemical evidence for a mantle plume beneath the Baikal rift zone. Journal of Petrology 46, 1309–1344.

Kepezhinskas, V.V., 1979. Cenozoic Alkaline Basalts of Mongolia and Related Deep Seated Inclusions, vol. 1–312. Nauka, Novosibirsk (in Russian).

Kiselev, A.I., 1987. Volcanism of the Baikal rift zone. Tectonophysics 143, 235–244.

Kalfoun, F., Ionov, D., Merlet, C., 2002. HFSE residence and Nb/Ta ratios in metasomatised, rutile-bearing mantle peridotites. Earth and Planetary Science Letters 199, 49–65.

Knutson, J., Green, T.H., 1975. Experimental duplication of a high-pressure megacryst/cumulate assemblage in a near-saturated hawaiite. Contributions to Mineralogy and Petrology 52, 121–132.

Kogiso, T., Hirose, K., Takahashi, E., 1998. Melting experiments on homogeneous mixtures of peridotite and basalt: application to the genesis of ocean island basalts. Earth and Planetary Science Letters 162, 45–61.

Kopylova, M.G., Nowell, G.M., Pearson, D.G., Markovic, G., 2009. Crystallization of megacrysts 1 from protokimberlitic fluids: geochemical evidence from high-Cr megacrysts in the Jericho kimberlite. Lithos 112 SP1, 284–295.

Kovács, I., Zajacz, Z., Szabó, C., 2004. Type-II xenoliths and related metasomatism from the Nógrád-Gömör Volcanic Field, Carpathian–Pannonian region (northern Hungary–southern Slovakia). Tectonophysics 393, 139–161 (Original Research Article).

Kovalenko, V.I., Solovova, I.P., Ryabchikov, I.D., Ionov, D.A., Bogatikov, O.A., 1987. Fluidized CO_2–sulphide–silicate media as agents of mantle metasomatism and megacrysts formation: evidence from a large druse in a spinel-lherzolite xenolith. Physics of the Earth and Planetary Interiors 45, 280–293.

La Tourrette, T., Hervig, R.L., Holloway, J.R., 1995. Trace element partitioning between amphibole, phlogopite, and basanite melt. Earth and Planetary Science Letters 135, 13–30.

Lavrent'ev, Y.G., Usova, L.V., Kuznetsova, A.I., Letov, S.V., 1987. X-ray spectral quant metric microanalysis of the most important minerals of kimberlites. Russian Geology and Geophysics 48 (5), 75–81.

Lavrent'ev, Yu.G., Usova, L.V., 1994. New version of KARAT program for quantitative X-ray spectral microanalysis. Zhurnal Analiticheskoi Khimii 5, 462–468.

Lee, D.C., Halliday, A.N., Davies, G.R., Essene, E.J., Fitton, J.G., Temdjim, R., 1996. Melt enrichment of shallow depleted mantle: a detailed petrological, trace element and isotopic study of mantle derived xenoliths and megacrysts from the Cameroon line. Journal of Petrology 37, 415–441.

Lee, C.-T., Rudnick, R.L., Brimhall, G.H., 2001. Deep lithospheric dynamics beneath the Sierra Nevada during the Mesozoic and Cenozoic as inferred from xenolith petrology. Geochemistry, Geophysics, Geosystems. V.2 N.GC000152.

Liotard, J.M., Briot, D., Boivin, P., 1988. Petrological and geochemical relationships between pyroxene megacrysts and associated alkali basalts from Massif Central (France). Mineralogy and Petrology 98, 81–90.

Litasov, K.D., Foley, S.F., Litasov, Yu.D., 2000. Magmatic modification and metasomatism of the subcontinental mantle beneath the Vitim volcanic field East Siberia : evidence from trace element data on pyroxenite and peridotite xenoliths from Miocene picrobasalt. Lithos 54, 83–114.

Liu, C.-Q., Masuda, A., Xie, G.-H., 1992. Isotope and trace-element geochemistry of alkali basalts and associated megacrysts from the Huangyishan volcano, Kuandian, Liaoning, NE China. Chemical Geology 97, 219–231.

Lorand, J.P., 1989. Sulfide petrology of spinel and garnet pyroxenite layers from mantle-derived spinel lherzolite massifs of arieg, northeastern Pyrenees, France. Journal of Petrology 30, 987–1015.

McDonough, W.F., Sun, S.S., 1995. The composition of the earth. Chemical Geology 120, 223–253.

Menzies, M.A., Kempton, P.D., Dungan, M., 1985. Interaction of continental lithosphere and asthenospheric melts below Geronimo volcanic field, Arizona. USA Journal of Petrology 26, 663–694.

Mysen, B.O., Boettcher, A.L., 1975. Melting of a hydrous mantle: I. Phase relations of natural peridotite at high pressures and temperatures with controlled activities of water, carbon dioxide, and hydrogen. Journal of Petrology 16, 520–548.

Mukhopadyay, B., Manton, W.I., 1994. Upper mantle fragments from beneath the Sierra Nevada batholith: partial fusion, fractional crystallization and metasomatism in a subduction-enriched ancient lithosphere. Journal of Petrology 35, 1418–1450.

Neal, C.R., 1995. The relationship between megacrysts and their host magma and identification of the mantle source region. EOS Transactions 76, 664.

Neal, C.R., Davidson, J.P., 1989. An unmetasomatized source for the Malaitan Alnoite (Solomon Islands); petrogenesis involving zone refining, megacryst fractionation, and assimilation of oceanic lithosphere. Geochimica et Cosmochimica Acta 53, 1975–1990.

Nimis, P., Taylor, W., 2000. Single clinopyroxene thermobarometry for garnet peridotites. Part I. Calibration and testing of a Cr-in-Cpx barometer and an enstatite-in-Cpx thermometer. Contributions to Mineralogy and Petrology 139, 541–554.

Nixon, P.H., Boyd, F.R., 1979. Garnet bearing lherzolites and discrete nodule suites from the Malaita alnoite, Solomon Islands, S.W. Pacific, and their bearing on oceanic mantle composition and geotherm. In: Boyd, F.R., Meyer, H.O.A. (Eds.), The mantle sample inclusions in kimberlite and other volcanics. AGU Washington. pp. 400–423.

O'Reilly, S.Y., Griffin, W.L., 1985. A xenolith derived geotherm for southeastern Australia and its geological implications. Tectonophysics 111, 41–63.

O'Reilly, S.Y, Griffin, W.L. 1990. Megacryst–basalt relationships: isotopic constraints. In: 7th lnternat Conference on Geochronology Cosmochronology and Isotope Geology, Canberra, p. 73.

Pearson, D.G., Nowell, G.M., 2004. Re–Os and Lu–Hf isotope constraints on the origin and age of pyroxenites from the Beni Bousera peridotite massif; implications for mixed peridotite–pyroxenite mantle sources. Journal of Petrology 45, 439–455.

Pivin, M., Féménias, O., Demaiffe, D., 2009. Metasomatic mantle origin for Mbuji–Mayi and Kundelungu garnet and clinopyroxene megacrysts (Democratic Republic of Congo). Lithos 112, 951–960.

Pouchou, J.L., Pichoir, F., 1984. A new model for quantitative X-ray microanalysis, Part I. Application to the analysis of homogeneous samples. Recherches Aerospace 3, 13–38.

Rankenburg, K., Lassiter, J.C., Brey, G., 2004. Origin of megacrysts in volcanic rocks of the Cameroon volcanic chain – constraints on magma genesis and crustal contamination. Contributions to Mineralogy and Petrology 147, 129–144.

Rankenburg, K., Lassiter, J.C., Brey, G., 2005. The role of continental crust and lithospheric mantle in the genesis of Cameroon Volcanic Line lavas: constraints from isotopic variations in lavas and megacrysts from the Biu and Jos Plateaux. Journal of Petrology 46, 169–191.

Rasskazov, S.V., Saranina, E.V., Logachev, N.A., et al., 2002. The DUPAL mantle anomaly of the Tuva–Mongolian massif and its paleogeodynamic implication. Doklady Akademii Nauk 382, 110–114.

Richard, P., Shimizu, N., Allègre, C.J., 1976. $^{143}Nd/^{144}Nd$, a natural tracer: an application to oceanic basalts. Earth and Planetary Science Letters 31, 269–278.

Righter, K., Carmichael, I.S.E., 1993. Mega-xenocrysts in alkali olivine basalts: fragments of disrupted mantle assemblages. American Mineralogist 78, 1230–1245.

Rollinson, H.R., 1993. Using Geochemical Data: Evaluation, Presentation, Interpretation. Longman, Harlow, England. 290pp.

Rosenbaum, J.M., 1992. Mantle phlogopite: a significant lead repository? Chemical Geology 106, 475–483.

Rudnick, R.L., Fountain, D.M., 1995. Nature and composition of the continental crust: a lower crustal perspective. Reviews of Geophysics 33, 267–309.

Schmidt, K.H., Bottazzi, P., Vannucci, R., Mengel, K., 1999. Trace element partitioning between phlogopite, clinopyroxene and leucite lamproite melt. Earth and Planetary Science Letters 168, 287–300.

Shaw, C.S.J., Eyzaguirre, J., 2000. Origin of megacrysts in the mafic alkaline lavas of the West Eifel volcanic field, Germany. Lithos 50, 75–95.

Sobolev, S.V., Siplivets, 1987. Evolution of the system magmatic reservoir–magmatic fracture. Transactions (Dokl) of the USSR Academy of Sciences 297 (5), 1667–1678.

Sobolev, A.V., Hofmann, A.W., Sobolev, S.V., Nikogosian, I.K., 2005. An olivine-free mantle source of Hawaiian shield basalts. Nature 434, 590–597.

Stalder, R., Foley, S.F., Brey, G.P., Horn, I., 1998. Mineral-aqueous fluid partitioning of trace elements at 900–1200 C and 3.0–5.7 GPa: new experimental data for garnet, clinopyroxene and rutile and implications for mantle metasomatism. Geochimica et Cosmochimica Acta 62, 1781–1801.

Stern, C.R., Kilian, R., Olker, B., Hauri, E.H., Kyser, T.K., 1999. Evidence from mantle xenoliths for relatively thin 100 km continental lithosphere below the Phanerozoic crust of southernmost South America. Lithos 48, 217–235.

Su, B.-X., Zhang, H.-F., Ying, J.-F., Xiao, Y., Zhao, X.-M., 2009. Nature and processes of the lithospheric mantle beneath the western Qinling: evidence from deformed peridotitic xenoliths in Cenozoic kamafugite from Haoti, Gansu Province. Journal of Asian Earth Sciences 31, 258–274.

Taylor, W.R., 1998. An experimental test of some geothermometer and geobarometer formulations for upper mantle peridotites with application to the thermobarometry of fertile lherzolite and garnet websterite. Neues Jahrbuch für Mineralogie, Abhandlungen 172, 381–408.

Thompson, R.N., 1972. Melting Behavior of Two Snake River Basalts at Pressures up to 35 kbars, vol. 71. Carnegi. Inst. Washington Yearb., pp. 406–410.

Upton, B.G.J., Hinton, R.W., Aspen, P., Finch, A., Valley, J.W., 1999. Megacrysts and Associated Xenoliths: evidence for migration of geochemically enriched melts in the upper mantle beneath Scotland. Journal of Petrology 40, 935–956.

Upton, B.G.J., Aspen, P., Hinton, R., 2003. Garnet pyroxenite xenoliths and pyropic megacrysts in Scottish alkali basalts. Scottish Journal of Geology 39, 169–184.

Verma, S.P., Besch, T., Guevara, M., Dobrich, B.S., 1992. Determination of twelve trace elements in twenty-seven and ten major elements in twenty-three geochemical reference samples by X-ray fluorescence spectrometry. Geostandard Newsletter 16, 301–309.

Walter, M.J., 1998. Melting of garnet peridotite and the origin of komatiite and depleted lithosphere. Journal of Petrology 39, 29–60.

Wilshire, H.G., Shervais, J.W., 1975. Al-Augite and Cr-Diopside Ultramafic Xenoliths in Basaltic Rocks from Western United States. Physics and Chemistry of the Earth 9, 257–272.

Wilshire, H.G., Pike, J.E., Meyer, C.E., Schwarzman, E.C., 1980. Amphibole-rich veins in lherzolite xenoliths, Dish Hill and Deadmen Lake, California. American Journal of Science 280A, 76–593.

Witt-Eickschen, G., Kramm, U., 1998. Evidence for the multiple stage evolution of the subcontinental lithospheric mantle beneath the Eifel (Germany) from pyroxenite and composite pyroxenite/peridotite xenoliths. Contributions to Mineralogy and Petrology 131, 258–272.

Witt-Eickschen, G., Seck, H.A., Mezger, K., Eggins, S.M., Altherr, R., 2003. Lithospheric mantle evolution beneath the Eifel (Germany): Constraints from Sr–Nd–Pb isotopes and trace element abundances in spinel peridotite and pyroxenite xenoliths. Journal of Petrology 44, 1077–1095.

Wood, B.J., Blundy, J.D., 1997. A predictive model for rare earth element partitioning between clinopyroxene and anhydrous silicate melt. Contributions to Mineralogy and Petrology 129, 166–181.

Xia, Q.-K., Dallaib, L., Deloulec, E., 2004. Oxygen and hydrogen isotope heterogeneity of clinopyroxene megacrysts from Nushan Volcano, SE China. Chemical Geology 209, 137–151.

Yaxley, G.M., 2000. Experimental study of the phase and melting relations of homogeneous basalt + peridotite mixtures and implications for the petrogenesis of flood basalts. Contributions to Mineralogy and Petrology 139, 326–338.

Zack, T., Brumm, R., 1998. Ilmenite/ liquid partition coefficients for 26 trace elements determined through ilmenite/clinopyroxene partitioning in garnet pyroxenites. In: 7th International Kimberlite Conference. Extended Abstracts. Cape Town, 986-988.

Zheng, J.P., Griffin, W.L., Qi, L., O'Reilly, S.Y., Sun, M., Zheng, S., Pearson, N., Gaoc, J.F., Yua, C.M., Sua, Y.P., Tanga, H.Y., Liu, Q.S., Su, Y.P., Wu, X.L., 2009. Age and composition of granulite and pyroxenite xenoliths in Hannuoba basalts reflect Paleogene underplating beneath the North China Craton. Chemical Geology 264, 266–280.